Max-Planck-Institut für Festkörperforschung
Stuttgart

Ultrafast nonlinear effects in one-dimensional photonic crystals

Tilman Höner zu Siederdissen

Dissertation an der
Universität Stuttgart

Oktober 2007

Ultrafast nonlinear effects in one-dimensional photonic crystals

Von der Fakultät Mathematik und Physik
der Universität Stuttgart
zur Erlangung der Würde eines Doktors der
Naturwissenschaften (Dr. rer. nat.) genehmigte Abhandlung

vorgelegt von

Tilman Höner zu Siederdissen

aus Bielefed

Hauptberichter:	Prof. Dr. H. Giessen
Mitberichter:	Prof. Dr. P. Michler
Tag der mündlichen Prüfung:	17.Dezember 2007

Physikalisches Institut der Universität Stuttgart
2007

Zwei Dinge sind zu unserer Arbeit nötig:
Unermüdliche Ausdauer und die Bereitschaft,
etwas, in das man viel Zeit und Arbeit
gesteckt hat, wieder wegzuwerfen.
- Albert Einstein

Kurzfassung

Diese Arbeit beschäftigt sich mit der zeitlichen Dynamik der Wechselwirkung von Licht mit einer speziellen Klasse von Nanostrukturen, den sogenannten photonischen Kristallen. Der Fokus dieser Untersuchungen liegt auf nichtlinearen Phänomenen auf einer Zeitskala unterhalb einer Pikosekunde.

Photonische Kristalle sind Festkörper-Nanostrukturen mit einer räumlich periodischen dielektrischen Funktion. Sie beeinflussen die Propagation von Licht in einer analogen Weise, wie das periodische Gitterpotential eines Halbleiters oder Metalls auf die Bewegung von Elektronen wirkt. Diese Strukturen werden als ein-, zwei- bzw. dreidimensional bezeichnet, je nachdem in wie vielen Raumdimensionen eine Periodizität vorliegt.

Für diese Arbeit wurden zwei verschiedene Typen von eindimensionalen photonischen Kristallen untersucht: Halbleiter-Mehrfach-Quantenfilm-Bragg-Strukturen, die zu den resonanten photonischen Kristallen gehören, und metall-dielektrische photonische Kristalle. Für beide Materialsysteme werden sowohl die fundamentalen Licht-Materie-Wechselwirkungen als auch mögliche Anwendungen diskutiert.

Die Eigenschaften von Mehrfach-Quantenfilm-Bragg-Strukturen wurden mit Methoden der phasenaufgelösten Pulspropagation gemessen. Mehrere Licht-Materie-Wechselwirkungsregime von linearer Anregung bis zu Hochintensitätsphänomenen wie Selbstphasenmodulation wurden sehr detailliert analysiert. Dabei konnte eine klare Abgrenzung des Einflusses der Quantenfilme vom Einfluss des Volumenteils der Strukturen erreicht werden. Die Resultate stellen einen bedeutenden Beitrag zum fundamentalen Verständnis der Kopplung von Licht an Halbleiter-Nanostrukturen dar.

Die Experimente, die im Rahmen dieser Arbeit an eindimensionalen, metall-dielektrischen photonischen Kristallen durchgeführt wurden, sind als Pionierarbeit anzusehen, da sie sich zum ersten Mal mit der zeitlichen Dynamik solcher

Strukturen beschäftigen. Diese Strukturen sind besonders interessant für Anwendungen im Bereich ultraschneller optischer Bauelemente. Mehrere Vorhersagen über deren Transmissionsdynamik konnten in den hier präsentierten Messungen überprüft werden. Im Wesentlichen wurden zwei Effekte auf verschiedenen Zeit- und Größenskalen beobachtet und ein signifikant abweichendes Verhalten im Vergleich zu einzelnen, wenige Nanometer dünnen Metallschichten gezeigt.

Abstract

This thesis deals with the temporal dynamics of light interacting with a special class of nano-structures: so-called photonic crystals (PCs). The focus of these investigations is nonlinear phenomena on a sub-picosecond time scale.

PCs are solid-state nano-structures with a spatially periodic dielectric function. They influence propagating light in an analogous manner to that of electronic motion in a periodic lattice potential of a semiconductor or metal. These structures are said to be one-, two-, or three-dimensional, depending on their spatial periodicity.

For this thesis, two different types of one-dimensional PCs have been studied: semiconductor multiple-quantum-well (MQW) Bragg structures, which are resonant PCs, and metal-dielectric PCs. For both material systems, the fundamental light-matter interaction processes, as well as potential applications, are discussed.

The properties of MQW Bragg structures have been investigated by phase-resolved pulse propagation measurements. Several light-matter interaction regimes, ranging from linear excitation to high-intensity phenomena such as self-phase modulation, have been studied in great detail. It has been possible to make a clear distinction between the bulk properties and the influence of the quantum wells. The results constitute a considerable contribution to the fundamental understanding of semiconductor nano-structures.

The experiments performed on one-dimensional metal-dielectric PCs are pioneering work in that they have studied the temporal dynamics in such structures for the very first time. These structures are especially interesting for application in ultrafast optical devices. Several predictions about their transmission dynamics could be tested in the measurements presented here. Essentially, two effects on different time and magnitude scales where observed, and a significantly different behavior as compared to single nano-scale metal layers could be identified.

Publications

Parts of this work have already been published:

In scientific journals:

- T. Höner zu Siederdissen, N. C. Nielsen, J. Kuhl, and H. Giessen, *Influence of near-resonant self-phase modulation on pulse propagation in semiconductors*, Journal of the Optical Society of America B **23**, 1360 (2006).

- T. Höner zu Siederdissen, N.C. Nielsen, J. Kuhl, M. Schaarschmidt, J. Förstner, A. Knorr, G. Khitrova, H.M. Gibbs, S.W. Koch, and H. Giessen *Transition between different coherent light-matter interaction regimes analyzed by phase-resolved pulse propagation*, Optics Letters **30**, 1384 (2005).

At scientific conferences:

- T. Höner zu Siederdissen, T. Ergin, J. Kuhl, M. Lippitz, and H. Giessen, *Ultrafast Nonlinear Switching Dynamics in Metallic Photonic Crystals* Frontiers in Optics 2007, Postdeadline Paper D2, San Jose, USA (2007).

- T. Höner zu Siederdissen, N. C. Nielsen, J. Kuhl, M. Schaarschmidt, A. Knorr, G. Khitrova, H. M. Gibbs, S. W. Koch, H. Giessen, *Phase-resolved nonlinear propagation: Transition between coherent light-matter interaction regimes*, Nonlinear Guided Waves and Their Applications (NLGW 2005), talk TuA4, Dresden, Germany (2005).

- T. Höner zu Siederdissen, N. C. Nielsen, J. Kuhl, M. Schaarschmidt, A. Knorr, and H. Giessen, *Ultrafast phase-resolved spectroscopy on semiconductor multiple-quantum-well Bragg structures in different lightmatter interaction regimes*,

69. Annual Meeting of the Deutsche Physikalische Gesellschaft (DPG), talk HL 63.4, Berlin, Germany (2005).

Additional scientific publications which are not presented in this thesis:

In scientific journals and books:

- N. C. Nielsen, T. Höner zu Siederdissen, J. Kuhl, M. Schaarschmidt, J. Förstner, A. Knorr, S. W. Koch, and H. Giessen,
  Temporal and Spatial Pulse Compression in a Nonlinear Defocusing Material,
  in "'Ultrafast Phenomena XIV," Eds. T. Kobayashi, T. Okada, T. Kobayashi, K. Nelson, and S. de Silvestri, Springer Verlag Heidelberg, p. 19 (2005).

- N.C. Nielsen, T. Höner zu Siederdissen, J. Kuhl, M. Schaarschmidt, J. Förstner, A. Knorr, and H. Giessen,
  Phase evolution of solitonlike optical pulses during excitonic Rabi flopping in a semiconductor,
  Physical Review Letters **94**, 057406 (2005).

- M. Breede, T. Höner zu Siederdissen, J. Kovacs, J. Struckmeier, J. Zimmermann, R. Hoffmann, M. Hofmann, T. Kleine-Ostmann, P. Knobloch, M. Koch, and J.P. Meyn,
  Semiconductor laser with simultaneous tunable dual wavelength emission,
  in "'Physics and Simulation of Optoelectronic Devices X", Eds. Peter Blood, Marek Osinski and Yasuhiko Arakawa, Proceedings of SPIE, Vol. 4646, p. 439 (2002).

At scientific conferences:

- T. Höner zu Siederdissen, N. C. Nielsen, J. Kuhl, J. Förstner, A. Knorr, and H. Giessen,
  Temporal phase evolution during excitonic Rabi flopping in semiconductors,
  International Quantum Electronics Conference (IQEC), talk IMB3, San Francisco, USA (2004).

- N. C. Nielsen, T. Höner zu Siederdissen, J. Kuhl, M. Schaarschmidt, J. Förstner, A. Knorr, S. W. Koch, and H. Giessen,
  Subpicosecond spatiotemporal pulse compression in a nonlinear defocusing material,
  14th International Conference on Ultrafast Phenomena (UP 2004), talk FA8, Niigata, Japan (2004).

- M. Breede, T. Höner zu Siederdissen, M.R. Hofmann, S. Hoffmann, J. Kovacs, J. Struckmeier, J. Zimmermann, T. Kleine-Ostmann, P. Knobloch, and M. Koch,
  Semiconductor laser with simultaneous tunable dual wavelength emission,
  SPIE Photonics West, San Jose, USA (2002).

Contents

Chapter 1
Introduction

Recent years and decades have seen tremendous progress in electronics. Especially in transistors—probably the most important elements of today's electronics—having shown great advance in operation speed and constant reduction of size. Modern microprocessors contain more than a billion transistors[1]. However, considering the development of single electron transistors [1], seemingly insurmountable physical limits begin to become relevant. To overcome these limitations, other concepts are required which do not depend on the constraints of electrons.

Photonics, the science and technology of photons, is very promising in this respect given that light travels much faster than electrons, and optical pulses can be considerably shorter than electric pulses. The generation of light pulses has become a relatively easy task due to a wide range of lasers presently available commercially. However, the development of reliable components to manipulate and route laser pulses in a way comparable to integrated electronic circuits still pose great challenges.

Photonic crystals (PCs)[2] are nano-structures with a spatially periodic dielectric function (or likewise refractive index). They influence propagating light in an analogous manner to that of electronic motion in a periodic lattice potential of a semiconductor (SC) or metal. Thus, they certainly constitute one of the most important concepts for controlled light manipulation. PCs are said to be one-, two-, or three-dimensional, depending on their spatial periodicity.

In this thesis, investigations of two variants of one-dimensional (1D) PCs will be presented: SC multiple-quantum-well (MQW) Bragg structures, which are resonant PCs, and metal-dielectric PCs. For both systems, the fundamental

[1] according to Intel®, an Itanium® 2 Dual-Core processor has about 1.7 billion transistors

[2] A list of acronyms can be found in appendix A

light-matter interaction processes will be discussed. Additionally, the feasibility of potential applications will be reviewed.

The most basic type of a 1D PC is a dielectric Bragg grating which consists of alternating non-resonant layers forming a 1D photonic band gap [2]. Prominent examples of this are fiber Bragg gratings [3, 4]. However, a pure dielectric PC offers very limited possibilities to selectively alter the optical properties other than at the time of fabrication. Introducing structures with periodically arranged resonances is much more promising in this respect. For this reason, MQW Bragg structures have been designed. It has been shown that they feature an ultrafast recovery effect showing great potential for developing a mirror with terahertz switching rates that either reflects or transmits a pulse [5, 6]. An array of such switches could redirect an incoming pulse into an arbitrary direction and perform so-called "optical packet switching" operations. Another possible application for MQW Bragg structures is pulse shaping, i.e., controlled manipulation of the temporal pulse profile upon propagation. In this field, especially the concept of solitons–pulses which maintain a stable shape during propagation–must be mentioned. So-called gap solitons have been predicted to exist in resonant PCs [7, 8], but recent studies [9] have shown that they cannot be expected in SC MQW Bragg structures due to the break-down of the photonic band gap at moderately high pulse intensities. Signatures of self-induced transmission and self-phase modulation (SPM) have been found in these investigations, leaving several open questions: What effects occur for even higher intensities and which role do the quantum wells (QWs) play in the intensity regimes where the band gap is strongly suppressed? How is the pulse phase influenced by the dynamics in the MQW structure? Can solitons other than gap solitons or soliton-like phenomena be observed?

The investigations presented in chapter 2 will show a comprehensive investigation of modifications to sub-picosecond pulses after propagation through a SC MQW Bragg structure. Additionally, a detailed study on propagation in bulk SCs will be presented to allow for a clear distinction between QW-induced effects and effects dominantly caused by the bulk part of such a structure. The applied measurement technique is based on a sophisticated fast-scanning cross-correlation frequency-resolved optical gating (XFROG) [10] scheme, which yields amplitude and phase of the measured laser pulses with a remarkably high signal-to-noise ratio.

The second material system investigated in this thesis are one-dimensional metal-dielectric photonic crystals (1DMDPCs), which have considerable advantages over the SC MQW structures. The SC structures require low temperatures, on the order of 10 K, to show the desired effects. In 1DMDPCs, the phenomena utilized to influence the material properties by light pulses are far less dependent on the environmental temperature. Thus, they can be used at room temperature. Secondly, the number of layers needed to achieve the desired effects is considerably lower. While SC MQW Bragg structures typically contain 60-200 QWs [5, 9], 1DMDPCs usually only need 5 metal layers [11]. Recent literature [11–17] indicate a high potential of 1DMDPCs for ultrafast all-optical switching applications. Nonetheless, experimental verifications for this are lacking since only static experiments have been made. The work presented in chapter 3 constitutes the first experimental time-resolved studies on the transmission dynamics in 1DMDPCs under strong pulsed laser pumping. The primary measurement technique employed for this is pump-probe spectroscopy with sub-picosecond time resolution. The results obtained by this method will provide new insight into the fundamental dynamics of periodically arranged metal layers and reveal strengths and weaknesses of this concept with respect to ultrafast all-optical switching applications.

Chapter 2
Pulse propagation in semiconductor multiple-quantum-well structures and bulk semiconductors

Interaction of propagating ultrashort laser pulses with semiconductor (SC) structures is of major interest from a scientific as well as a technical point of view. SC materials certainly play a crucial role in current and future technologies, e.g., those based on all-optical switching [6, 18] or quantum information processing [19–21]. To obtain a complete understanding of pulse modifications induced by the material, it is important to determine not only the field intensity but also its phase [22]. This phase information is vital to identify output pulse properties such as chirp or relations between split-off pulse components, for example phase jumps. So far, most experiments in SC optics have neglected the phase. Recent experiments [23–25] have clearly shown that its knowledge gives new insight into different light-matter interaction regimes such as polariton beating in bulk SCs, self-induced transmission in SCs, and self-phase modulation (SPM) soliton formation in optical fibers.

In this chapter, a comprehensive study of several fundamental light-matter interaction regimes in an (In, Ga)As/GaAs multiple-quantum-well (MQW) Bragg structure at low temperature is provided. The knowledge of pulse amplitude and phase allows to clearly identify the involved linear and nonlinear effects. Due to the fact that the investigated phenomena occur in many different material systems in an analogous way, the knowledge gained from these observations is relevant beyond the material system used here. To gather the relevant experimental

data, phase-resolved sub-picosecond pulse propagation measurements based on a fast-scanning cross-correlation frequency-resolved optical gating (XFROG) setup have been performed on the MQW Bragg structure. This measurement technique has been developed to achieve an excellent signal-to-noise ratio and low retrieval errors of the XFROG algorithm. The experimental findings are compared with calculations solving the semiconductor Maxwell-Bloch equations (SMBE) in collaboration with M. Schaarschmidt, J. Förstner, and A. Knorr from the Technische Universität Berlin and S. W. Koch from the Philipps-Universität Marburg. The MQW Bragg structure qualifies as a one-dimensional (1D) *resonant* photonic crystal (PC), as the excitons in the quantum wells (QWs) are resonant to the exciting light and as it exhibits a periodic variation of the complex refractive index. In this specific case, the lowest heavy-hole exciton resonance is used. The studies presented here cover the complete intensity range from linear propagation to the breakdown of the photonic band gap (PBG) [6] due to increasing nonlinear excitation, on to self-induced transmission [9, 26], and up to the strong SPM regime [27]. They include investigations at substantially higher intensities than previous publications on MQW Bragg structures [9] and SPM soliton formation [25], which show comparable effects as observed in the low and intermediate intensity regime.

Purely from the measurements of the MQW Bragg structure alone, it is not possible to distinguish between effects governed by the quantum wells and those caused by the GaAs bulk substrate and the spacer layers. To fully understand the processes in such structures, experiments without quantum wells are needed for comparison. (Measurements without the substrate and the spacer layers are presumed to be technically not feasible.) Therefore, also a detailed analysis of near-resonant sub-picosecond pulse propagation through bulk GaAs at low temperature is given. These investigations are not only interesting for the comparison with the MQW results, but also considerably contribute to the fundamental knowledge about ultrafast light-matter interaction in bulk SC crystals. Closely below the band gap, GaAs exhibits normal dispersion and a negative Kerr nonlinearity. This is one of two regimes where bright solitons are generally possible, although the occurrence of solitons in the opposite regime (anomalous dispersion and a positive Kerr nonlinearity) is better known in optical fibers. Previous investigations in SCs have shown self-steepening [28] and soliton-like pulse compression [29]. In this work, the dependence of the pulse characteristics on

the propagation length, the input pulse intensity, the focusing into the sample, and the detuning from the band edge are covered. The results of phase-resolved measurements are used to characterize the evolution of the pulse amplitude and phase during propagation. These experiments are also based on the fast-scanning technique that ensures high signal-to-noise ratios. Numerical simulations based on the nonlinear Schrödinger equation (NLSE) have been made and are compared with the experimental observations.

Many of the results contained in this chapter have already been published in Refs. [30] and [31].

2.1. Theoretical background

In this section, a brief introduction to the NLSE and the term *soliton* is given.

2.1.1. The nonlinear Schrödinger equation

In the following, the derivation of the NLSE is sketched for propagation of short pulses in optical fibers. Later (section 2.4.3), it will be shown that this equation (with small modifications) also works well for propagation in bulk SCs. The same notations as in Ref. [32] are used.

Light propagation in solid state media is governed by Maxwell's equations for the electric and magnetic field vectors $\mathbf{E}$ and $\mathbf{H}$:

$$\nabla \times \mathbf{E} = -\frac{\partial \mathbf{B}}{\partial t}, \tag{2.1}$$

$$\nabla \times \mathbf{H} = \mathbf{J} + \frac{\partial \mathbf{D}}{\partial t}, \tag{2.2}$$

$$\nabla \cdot \mathbf{D} = \rho_f, \tag{2.3}$$

$$\nabla \cdot \mathbf{B} = 0. \tag{2.4}$$

Here, $\mathbf{D}$ and $\mathbf{B}$ are the electric and magnetic flux densities, $\mathbf{J}$ the current density vector, and ρ_f the charge density. In absence of free charges, the latter two vanish. The flux densities are given by the sums of the external fields (times the vacuum permittivity/permeability) and the induced electric and magnetic

material polarizations $\mathbf{P}$ and $\mathbf{M}$:

$$\mathbf{D} = \epsilon_0 \mathbf{E} + \mathbf{P}, \tag{2.5}$$

$$\mathbf{B} = \mu_0 \mathbf{H} + \mathbf{M}. \tag{2.6}$$

Only non-magnetic media with $\mathbf{M} = 0$ are considered in the following. Using these relations and taking the curl of equation 2.1 leads to

$$\nabla \times \nabla \times \mathbf{E} = -\frac{1}{c^2}\frac{\partial^2 \mathbf{E}}{\partial t^2} - \mu_0 \frac{\partial^2 \mathbf{P}}{\partial t^2} \tag{2.7}$$

with the vacuum speed of light $c = (\mu_0 \epsilon_0)^{-1/2}$. To solve this equation, the relation between the electric field $\mathbf{E}$ and the material polarization $\mathbf{P}$ is needed. This relation is commonly approximated by a power series of a certain order N, i.e., a certain maximum power of the electric field $\mathbf{E}$:

$$\mathbf{P} = \epsilon_0 \sum_{j=1}^{N} \chi^{(j)} \mathbf{E}^j. \tag{2.8}$$

The case $N = 1$ is considered as linear optics, all further terms describe nonlinear effects. $\chi^{(j)}$ is called the j^{th} order susceptibility.

To derive the NLSE in a form that is valid for optical fibers, the following approximations are made:

- The medium is isotropic, thus having inversion symmetry and therefore $\chi^{(2)} = 0$.
- All terms higher than the third order are very small and can be neglected. Therefore, the polarization consists of only two parts, the linear and the third order nonlinear term:

$$\mathbf{P}(\mathbf{r}, t) = \mathbf{P}_L(\mathbf{r}, t) + \mathbf{P}_{NL}(\mathbf{r}, t) \tag{2.9}$$

- The electric field and the polarization are linearly polarized and the medium maintains the polarization. Based on this, it suffices to treat the electric field as a scalar.
- Contribution from molecular vibrations (Raman effect) are neglected. This is reasonable since the response of the nuclei is inherently smaller than the electronic response.

- All effects that require phase matching such as third harmonic generation are assumed to be negligibly small.
- The nonlinear contribution to the polarization $\mathbf{P}_{NL}$ is treated as a small perturbation compared to the dominant linear part of the polarization $\mathbf{P}_L$.
- Slowly varying envelope approximation: The electric field is quasi-monochromatic ($\Delta\omega \ll \omega_0$) and can be written in the form

$$\mathbf{E} = \frac{1}{2}\hat{x}\left[E(\mathbf{r},t)\exp(-i\omega_0 t) + c.c.\right]. \tag{2.10}$$

  The linear and nonlinear polarization can be written in a similar way by replacing E with P_L or P_{NL}.

It follows that the nonlinear polarization can be simplified to

$$P_{NL}(\mathbf{r},t) = \epsilon_0 \epsilon_{NL} E(\mathbf{r},t) \tag{2.11}$$

with

$$\epsilon_{NL} = \frac{3}{4}\chi^{(3)}_{xxxx}|E(\mathbf{r},t)|^2. \tag{2.12}$$

To obtain the wave equation for $E(\mathbf{r},t)$, it is convenient to switch to the frequency domain by applying a Fourier transform[1]. Due to the slowly varying envelope approximation and the perturbative nature of P_{NL}, ϵ_{NL} is treated as a constant in this step. At first, the Fourier transformation of Eq. (2.7) is calculated for $P_{NL} = 0$ before reintroducing ϵ_{NL}:

$$\nabla \times \nabla \times \tilde{\mathbf{E}}(\mathbf{r},\omega) = \epsilon(\omega)\frac{\omega^2}{c^2}\tilde{\mathbf{E}}(\mathbf{r},\omega) \tag{2.13}$$

with $\epsilon(\omega) = 1+\tilde{\chi}^{(1)}(\omega)$. Assuming that ϵ is independent of the spatial coordinates, the relation

$$\nabla \times \nabla \times \mathbf{E} = \nabla(\nabla \times \mathbf{E}) - \nabla^2\mathbf{E} = -\nabla^2\mathbf{E} \tag{2.14}$$

can be applied and Eq. (2.13) takes the form of the Helmholtz equation

$$\nabla^2\tilde{\mathbf{E}} + \epsilon(\omega)\frac{\omega^2}{c^2}\tilde{\mathbf{E}} = 0. \tag{2.15}$$

The Fourier transform of the electric field $\tilde{E}(\mathbf{r},\omega-\omega_0)$ is found to satisfy Eq. (2.15) for

$$\epsilon(\omega) = 1 + \tilde{\chi}^{(1)}_{xx}(\omega) + \epsilon_{NL}. \tag{2.16}$$

[1] the Fourier transform of a function F is denoted as $\tilde{F}$

To solve Eq. (2.15), a separation of variables can be used. The electric field is written in the form

$$\tilde{E} = F(x,y)\tilde{A}(z,\omega-\omega_0)\exp(i\beta_0 z), \tag{2.17}$$

where $\tilde{A}(z,\omega-\omega_0)$ is a slowly varying function of z and β_0 is the wave number, which is to be determined later. The corresponding time domain representation of the electric field is

$$E = \frac{1}{2}\hat{x}\left[F(x,y)A(z,t)\exp(i\beta_0 z - i\omega_0 t) + \text{c.c.}\right]. \tag{2.18}$$

The separation of variables approach leads to separate equations for the envelope $\tilde{A}$ and the transverse spatial profile F:

$$\frac{\partial^2 F}{\partial x^2} + \frac{\partial^2 F}{\partial y^2} + \left[\epsilon(\omega)\frac{\omega^2}{c^2} - \tilde{\beta}^2\right]F = 0 \tag{2.19}$$

$$2i\beta_0\frac{\partial \tilde{A}}{\partial z} + (\tilde{\beta}^3 - \beta_0^2)\tilde{A} = 0. \tag{2.20}$$

Here, the second derivative $\frac{\partial^2 \tilde{A}}{\partial z^2}$ in Eq. (2.20) is neglected because $\tilde{A}$ is assumed to be slowly varying with z. The wave number $\tilde{\beta}$ is determined by solving the eigenvalue equation (2.19), which can be solved by first order perturbation theory [32]. In a single mode fiber, $F(x,y)$ can be approximated by a Gaussian function

$$F(x,y) = e^{-(x^2+y^2)/w^2}, \tag{2.21}$$

where w is the spatial beam width. $\tilde{\beta}$ is now split into a term $\beta(\omega)$ independent of the spatial distribution F and a dependent term $\Delta\beta(\omega)$:

$$\tilde{\beta} = \beta(\omega) + \Delta\beta(\omega). \tag{2.22}$$

$\tilde{\beta}^2 - \beta_0^2$ is approximated by $2\beta_0(\tilde{\beta} - \beta_0)$. This results in the equation

$$\frac{\partial \tilde{A}}{\partial z} = i\left[\beta(\omega) + \Delta\beta(\omega) - \beta_0\right]\tilde{A}. \tag{2.23}$$

Now $\beta(\omega)$ and $\Delta\beta(\omega)$ are expanded into a Taylor series around the carrier frequency ω_0 as

$$\beta(\omega) = \beta_0 + (\omega-\omega_0)\beta_1 + \frac{1}{2}(\omega-\omega_0)^2\beta_2 + \frac{1}{6}(\omega-\omega_0)^3\beta_3 + ... \tag{2.24}$$

$$\Delta\beta(\omega) = \Delta\beta_0 + (\omega-\omega_0)\Delta\beta_1 + ... \tag{2.25}$$

with $\beta_0 = \beta(\omega_0)$ and $\beta_m = \left(\frac{d^m\beta}{d\omega^m}\right)_{\omega=\omega_0}$, analogous for $\Delta\beta_m$. Assuming $\Delta\omega \ll \omega_0$, the cubic and higher order terms in Eq. (2.24) can be neglected and $\Delta\beta$ simplified to

$$\Delta\beta(\omega) = \Delta\beta_0. \tag{2.26}$$

Going back to the time domain using the inverse Fourier transform (the term $(\omega - \omega_0)$ transforms into the differential operator $i\frac{\partial}{\partial t}$), the equation for $A(z,t)$ becomes

$$\frac{\partial A}{\partial z} + \beta_1\frac{\partial A}{\partial t} + \frac{i}{2}\beta_2\frac{\partial^2 A}{\partial t^2} = i\Delta\beta_0 A. \tag{2.27}$$

$\Delta\beta_0$ include the fiber loss (represented by the absorptions coefficient α) and the third order nonlinearity (nonlinear parameter $\gamma = \frac{2\pi n_2}{\lambda}$). Using $\beta(\omega) \approx n(\omega)\omega/c$ and assuming that $F(x,y)$ does not vary much over the pulse bandwidth, Eq. (2.27) takes the form

$$\frac{\partial A}{\partial z} + \beta_1\frac{\partial A}{\partial t} + \frac{i}{2}\beta_2\frac{\partial^2 A}{\partial t^2} + \frac{\alpha}{2}A = i\gamma(\omega)|A|^2 A. \tag{2.28}$$

The parameter β_1 corresponds to the inverse group velocity of the light pulse and can be eliminated by a transformation to $T = t - \beta_1 z$ into the moving frame. This results in the NLSE in the form which is used in section 2.4.3:

$$\frac{\partial A}{\partial z} = -\frac{\alpha}{2}A - \frac{i}{2}\beta_2\frac{\partial^2}{\partial T^2}A + i\gamma|A|^2 A. \tag{2.29}$$

The material parameters in this equation for the field envelope $A(z,T)$ are the absorption coefficient α, the group-velocity dispersion (GVD) parameter β_2, and the nonlinear parameter γ, which is related to the commonly used nonlinear refractive index n_2 (in units of the electric field: m^2/V^2) by $\gamma = \frac{2\pi n_2}{\lambda}$. Please note that in this thesis, γ is defined differently than in Ref. [32]. Instead of A beeing the optical power, A is given in units of the electric field. This is more consistent with the definition of A in Eq. (2.18) and the matches role of A as the envelope of the electric field. In this case, γ is a material constant independent of the geometrical properties of the fiber. The initial envelope function $A(0,T)$ is determined as follows:

Using the formalism of Ref. [33], the optical power of an electric field $\mathbf{E}$ is given by:

$$P(t) = \int_S I(t)dS, \tag{2.30}$$

where $I(t)$ is the intensity per unit area (W/cm^2)

$$I(t) = \frac{1}{2}\epsilon_0 cn|E(t)|^2. \tag{2.31}$$

Using definition (2.18) yields

$$P(t) = \int\int \frac{1}{2}\epsilon_0 cn|F(x,y)|^2|A(z,t)|^2 dxdy = \frac{1}{2}\epsilon_0 cn|A(z,t)|^2 \int\int |F(x,y)|^2 dxdy. \tag{2.32}$$

Eq. (2.21) and

$$\int\int \left| e^{-\frac{(x^2+y^2)}{w^2}} \right|^2 dxdy = \frac{\pi}{2}w^2 \tag{2.33}$$

deliver the relation between A and the optical power P:

$$P(t) = \frac{\pi}{4}w^2\epsilon_0 cn|A(z,t)|^2. \tag{2.34}$$

The pulse energy, which is known from the experiments, is related to the power by

$$E_{pulse} = \int_{-\infty}^{\infty} P(t')dt' \tag{2.35}$$

We assume an initially Gaussian shaped pulse

$$A(0,T) = A_0 \cdot e^{-\frac{T^2}{\tau_0^2}}, \tag{2.36}$$

where τ_0 is the temporal pulse length. Thus (with A transformed into the moving frame)

$$E_{pulse} = \int_{-\infty}^{\infty} \frac{\pi}{4}w^2\epsilon_0 cn|A(0,T')|^2 dT' = A_0^2 \frac{\pi w^2 \epsilon_0 cn\sqrt{\pi}\tau_0}{\sqrt{32}}. \tag{2.37}$$

Solving for the the initial maximum amplitude A_0 (in V/m) gives

$$A_0 = \sqrt{\frac{\sqrt{32}E_{pulse}}{\pi w^2 \epsilon_0 cn\sqrt{\pi}T_0}}. \tag{2.38}$$

Using this relation and Eq. 2.36, it is simple to determine the initial electric filed for solving the NLSE from the measured quantities: the temporal pulse length τ_0, the spatial beam width w, and the pulse energy E_{pulse}.

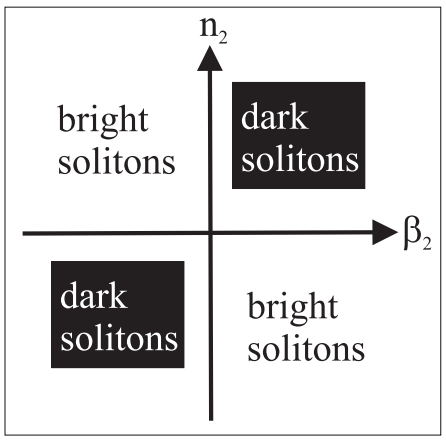

Figure 2.1.: Conditions for bright and dark solitons. β_2: GVD parameter, n_2: nonlinear refractive index.

2.1.2. Solitons

The term *soliton* in this thesis always refers to a fundamental bright soliton. Bright solitons are bright light pulses, in contrast to dark solitons which are dips in a uniform background. Fundamental solitons are pulses that maintain their shape while propagating through a medium. There are also so-called higher-order solitons which exhibit a periodic shape modulation during propagation. Both, dark and higher-order solitons are not relevant for this work.

To form a soliton, the processes in the medium that alter the pulse shape must be in balance and cancel each other out. For example, one effect broadens the pulse while another one causes a compression. Typically, one of the two effects is intensity dependent while the other is not. The main condition for the soliton then is the correct initial pulse intensity. To allow compensation of the GVD in a medium by SPM, the corresponding parameters β_2 and n_2 must have opposite signs. Closely below the band gap, a SC exhibits normal dispersion and a negative Kerr nonlinearity, i.e., $\beta_2 > 0$ and $n_2 < 0$. As depicted in Fig. 2.1, this condition potentially allows the formation of bright solitons. If β_2 and n_2 have the same sign, only dark solitons are possible, which are far less relevant for applications. Standard optical fibers usually have a positive Kerr nonlinearity and therefore only support bright solitons in anomalous dispersion regimes. The reason for the negative sign of the nonlinear refractive index n_2 close to the band gap in SCs is the so-called band gap renormalization [34]. This well-known phenomenon

arises from many-body interactions of free electrons. As optical excitations in SCs induce relatively high free carrier populations band gap renormalization is the dominant reason for optical nonlinearity. Exchange correlations of the free electrons reduce the band gap and thereby cause a decrease of the refractive index depending on the number of absorbed photons.

2.2. Experimental techniques and samples

The measurement technique used for the experiments presented in this chapter is based on a fast-scanning XFROG [10] scheme. Figure 2.2 illustrates the experimental setup which allows rapid, high signal-to-noise ratio acquisition of the shape, the spectrum, and the phase of pulses propagated through a given sample. A Ti:Sapphire oscillator that delivers 100 fs pulses centered at 830 or 836 nm at a repetition rate of 76 MHz serves as the light source. The linearly polarized laser output is divided into two portions by a beam splitter: The weaker part (about 1/3 of the power) enters a variable delay line, while the other part passes through a pulse shaper (consisting of a 4-f line with a reflective pulse shaper mask) to tailor pulses with a duration τ_p of approximately 600 fs, spectrally matched to the heavy hole 1s exciton resonance of the MQW sample. The shaped pulses are focused onto the sample with a $f = 25$ mm microscope objective. The sample itself is kept at a temperature of about 8-10 K in a cold-finger cryostat. The transmitted pulses are spectrally recorded or time-resolved by cross correlation with the temporally delayed 100 fs pulses in a 300-μm-thick β-barium-borate (BBO) crystal. The cross-correlation signal is detected with a photomultiplier tube (PMT) or dispersed in a spectrometer and recorded by a charge-coupled device (CCD) camera yielding the XFROG trace. A fast-scanning sampling technique to average over many scans for low-noise pulse acquisition [24, 35] is employed. This technique involves a stabilized shaker system which periodically modulates the pulse delay at a frequency of 60 Hz. A stepper motor is used to produce discrete delay shifts for the time-base calibration. For the XFROG measurements, a galvanometric scanning mirror is placed in front of the spectrometer slit that

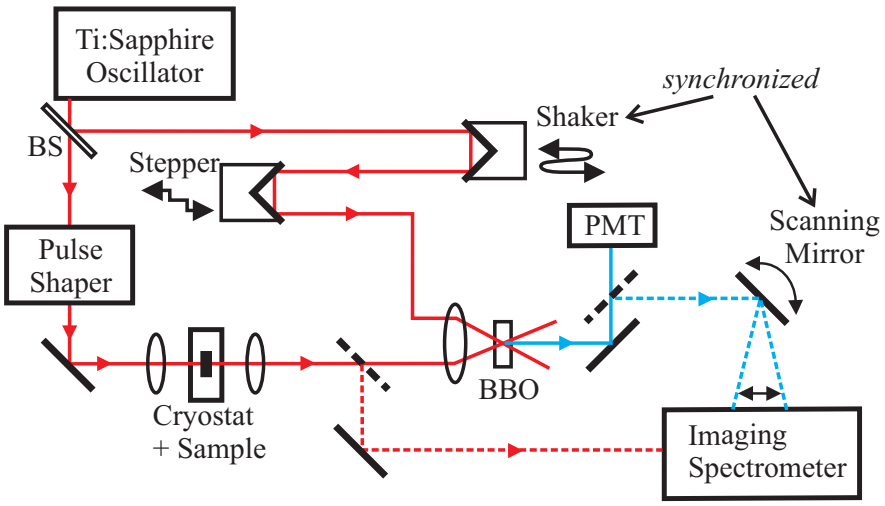

Figure 2.2.: Pulse propagation setup: The pulses from the Ti:Sapphire oscillator are split by a beam splitter (BS), shaped by a pulse shaper, and focused onto the sample. Afterwards, they can be directly measured by a spectrometer or superimposed with 100 fs reference pulses in a β-barium-borate (BBO) crystal. The resulting sum-frequency signal can be time-resolved by cross correlation (using a photomultiplier tube (PMT)) or phase-resolved by XFROG.

periodically scans the vertical beam position on the CCD array. This modulation is synchronized to the shaker in the delay line. The time-dependent intensity and phase of the pulse are retrieved by the XFROG algorithm [10], which typically achieves low retrieval errors of less than 0.003 on a 256×256 grid as a result of the high signal-to-noise ratio provided by the measurement technique.

The MQW sample has been epitaxially grown on a 450-μm-thick GaAs wafer and consists of 60 $In_{0.04}Ga_{0.96}As$ QWs with a thickness of 8.5 nm separated by GaAs barriers. The barrier thickness is monotonically increasing from one side of the sample to the other. This way the interwell distance d can be adjusted by changing the position of the laser excitation spot. For the lowest heavy-hole exciton resonance $\lambda_{ex} = 830$ nm and a refractive index $n_b \approx 3.65$ of the GaAs barrier material, the Bragg resonance is achieved at $d \approx 113.7$ nm. The front surface has been coated with an anti-reflection layer. The linear extinction spectra of this sample (DBR17) for resonant and off-resonant propagation are depicted in Fig. 2.3(a) as originally published in Ref. [9]. Furthermore, experiments have been performed on a series of bulk GaAs samples cut from the same single crystal

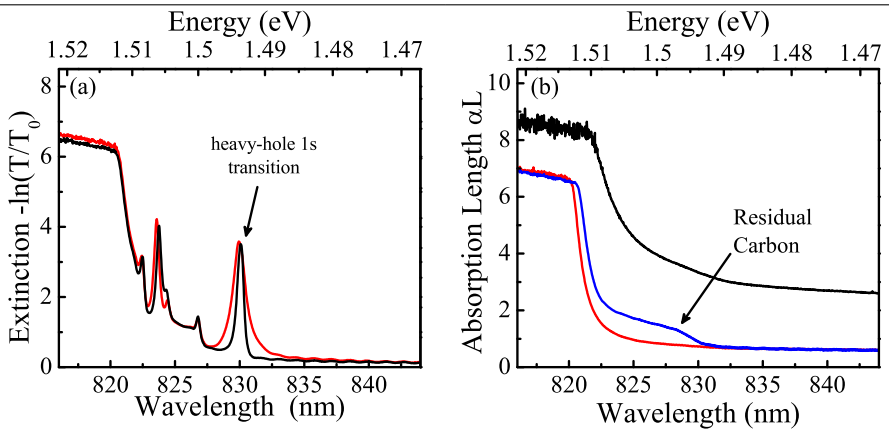

Figure 2.3.: (a) Linear extinction spectra of the antireflection-coated $N = 60$ (In,Ga)As/GaAs MQW structure at $T = 9$ K for $n_b d = 0.5\lambda_{ex}$ (black line) and $n_b d = 0.479\lambda_{ex}$ (red line). (b) Linear absorption spectra of the bulk samples with a thickness of 250 μm (red line) and 1000 μm (black line) cut from the same piece of bulk GaAs. Blue line: Linear absorption spectrum of the optically polished 600-μm-thick GaAs wafer used for the XFROG measurements.

with thicknesses between 250 μm and 2000 μm, varying in steps of 250 μm. The coplanar surfaces of the samples are oriented perpendicularly to the [100] crystal direction and have been polished to an optical grade. Figure 2.3(b) shows the corresponding absorption spectra (corrected for surface reflectivity) for the 250-μm- (red line) and 1000-μm-thick (black line) samples. The blue line shows the spectrum of an additional sample of eminently high quality, which is a piece of an optically polished 600-μm-thick GaAs wafer. There is an impurity band observable caused by residual carbon from the growth process, which extends from the Urbach tail at the fundamental band edge to about 830 nm. This sample is used for the XFROG experiments. It provides the best quality and therefore yields the highest possible signal-to-noise ratio which is important for an accurate retrieval of the pulse phase.

2.3. Pulse propagation in multiple-quantum-well Bragg structures

2.3.1. Experimental results

Figure 2.4 shows the results obtained by XFROG measurements on the MQW Bragg structure for different input intensities. The black line represents the normalized intensity, the red line represents the phase of the electric field versus time. The corresponding normalized spectra are shown in Fig. 2.5. The input pulse [Fig. 2.4(a)] exhibits a nearly constant phase over the pulse with slightly chirped outer wings. Due to the dispersion around the PBG, propagation at 0.2 MW/cm^2 results in two distinct pulse components with different carrier frequencies, i.e., linear phase segments with different slopes [22] in the time domain [Fig. 2.4(b)] and two peaks in the spectrum [Fig. 2.5(b)]. The temporal phase jump of π between the split-off pulse components confirms a propagation beating [9]: The exciton resonance is broadened by the superradiant coupling and forms a PBG that leaves two spectral wings from the input spectrum. The two spectral components transform into a temporal beating with π phase shifts between the pulse components. However, only one beat period is found due to the rapid radiative dephasing ($T_2 \approx 400$ fs) [9]. Increasing the input intensity results in suppression of the beating [Fig. 2.4(c)] and increased transmission at the exciton resonance [Fig. 2.5(c)]. The phase jump disappears and evolves into a steeply falling phase. This reflects the breakdown of the superradiant mode due to the Pauli-blocking nonlinearity and the adiabatically driven electron dynamics [6, 9] that gradually decouple the QW polarization from the light field for the time of the pulse duration. At 15 MW/cm^2 the output pulse with a flat phase leaves the sample essentially unaltered [Fig. 2.4(d)], presuming a decrease in pulse energy is neglected and a slight broadening induced by the dispersion of the 450 μm bulk substrate. The spectrum does not differ noticeably from the input spectrum. This phenomenon of self-induced transmission in SCs [9, 26] indicates that a full Rabi flop of the carrier density has occurred within the suppressed band gap of the MQW structure. Further increase of the intensity leads to SPM, which is immediately evident in spectral wings [Fig. 2.5(e)]. This initially forms a well-

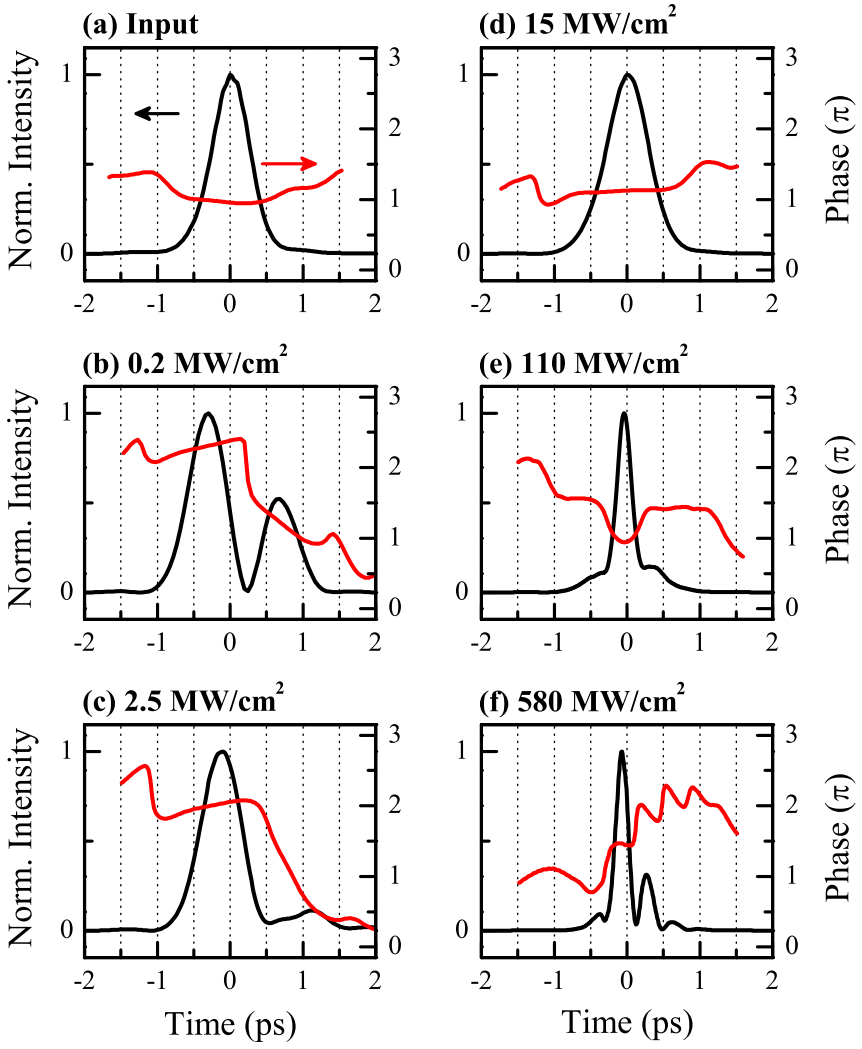

Figure 2.4.: Experimental XFROG results: Normalized intensity (black line) and phase (red line) versus time of the (a) input and (b)-(f) output pulses after propagation through the MQW Bragg structure for input intensities from 0.2 to 580 MW/cm^2.

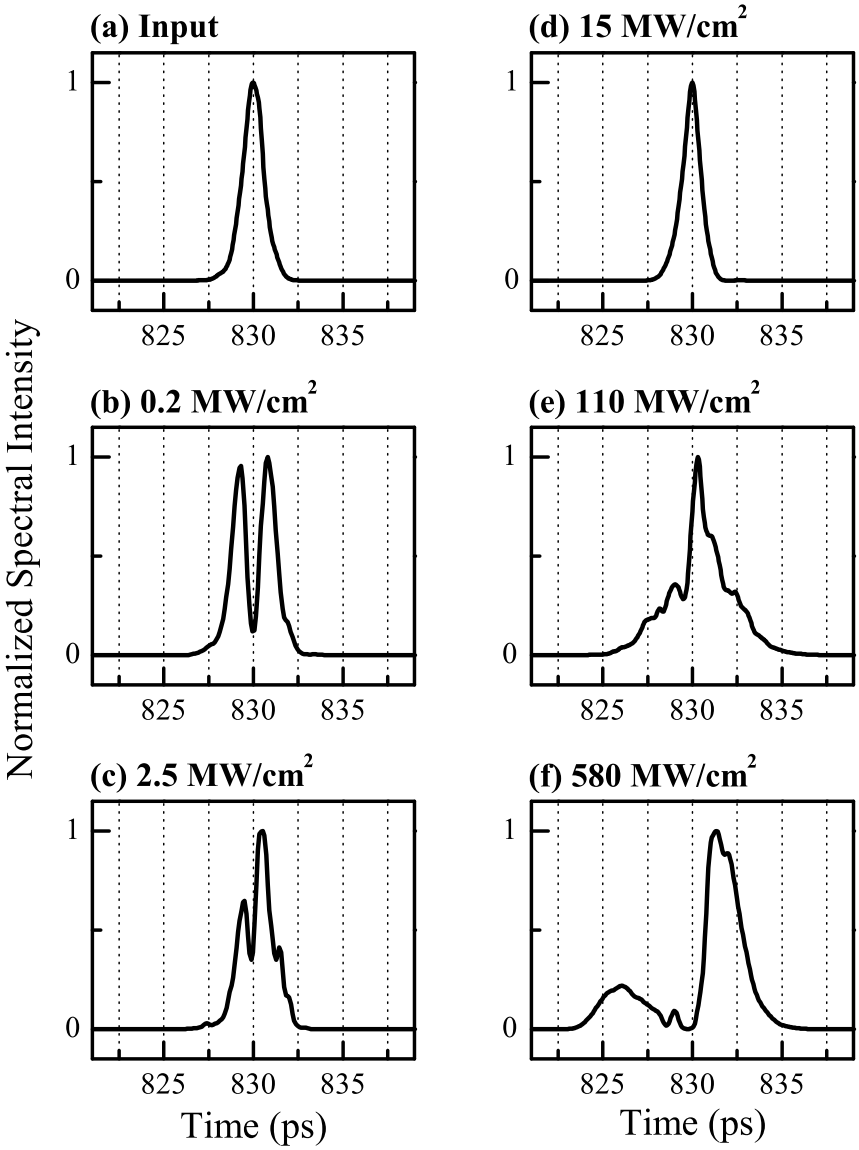

Figure 2.5.: Retrieved spectra corresponding to Fig. 2.4 of the (a) input and (b)-(f) output pulses after propagation through the MQW Bragg structure for input intensities from 0.2 to 580 MW/cm^2.

shaped phase around the main pulse [Fig. 2.4(e)], i.e., a steep phase at both sides of the main pulse (analogous to propagation in fibers [25] with switched signs of dispersion and Kerr nonlinearity). At even higher input intensities the spectrum is split into two components by strong SPM [Fig. 2.5(f)], and the pulse develops into a temporal pulse train [Fig. 2.4(f)]. The intensity of the spectral component closer to the band edge (smaller wavelengths) is lower due to reabsorption. The initial laser spectrum is strongly suppressed, i.e., converted into new frequency components. The separation between peaks of about 10 meV ($\Delta t \approx 400$ fs) corresponds to the temporal beating period of $\Delta t \approx 350$ fs. Small phase jumps ($\approx \pi/2$) can be seen between the subsequent pulses. Experiments in bulk GaAs yield the same pulse breakup but with full π phase jumps (see section 2.4.4). In this regime, the bulk effect of the substrate clearly dominates, while a zero crossing of the field (necessary for a full π phase jump) is prevented by the nonlinearly excited QWs. The main pulse in Fig. 2.4(f) has a flat phase, indicating soliton-like propagation. The excess energy forms the adjacent pulses which are too weak to fully compensate the dispersion and are therefore chirped or at least frequency shifted with respect to the incident pulse. A beating induced by the interplay of dispersion and nonlinearity has been called *modulational instability* in the literature [36], whereas the phase behavior rather suggests an "SPM beating". Measurements with an interwell distance detuned from the Bragg condition show more beating periods for linear excitation due to the increased dephasing time of several picoseconds. However, in the nonlinear regimes where the QW polarization is decoupled from the light field, there is no significant difference from the Bragg-resonant case.

2.3.2. Comparison with numerical calculations

The theoretical description of the light propagation effects requires splitting the sample into MQW structure and bulk wafer. For resonant propagation in the MQW, the transmitted signal is calculated by numerically solving the SMBE in the Hartree-Fock limit [37] using the finite-difference time-domain method [6, 38]. This method allows the calculation of multiple reflection, back-reflection, and light propagation in both directions and reproduces the formation and suppression of the PBG as shown in Ref. [6]. For the subsequent off-resonant propaga-

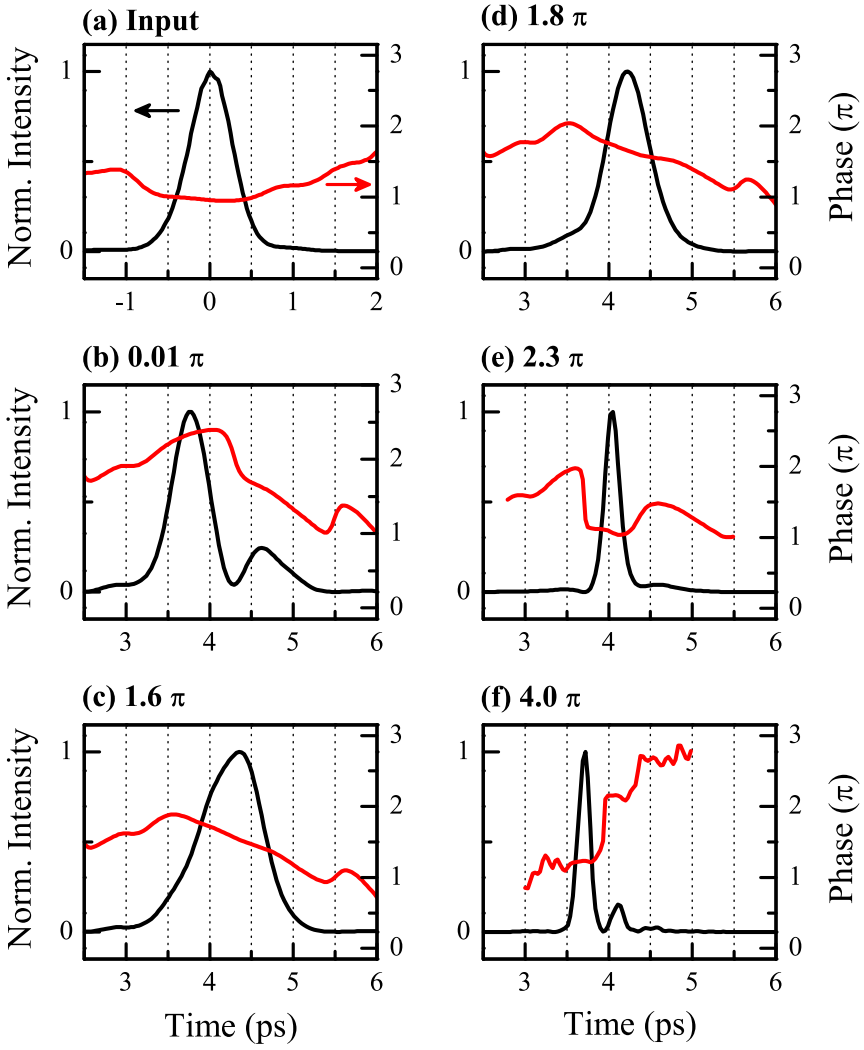

Figure 2.6.: Numerical calculations: Normalized intensity (black line) and phase (red line) versus time of the (a) input and (b)-(f) output pulses after propagation through the MQW Bragg structure for input pulse areas from 0.01 π to 4 π.

tion through the bulk SC below the excitonic resonance, Maxwell's equations are evaluated using the slowly varying envelope approximation [39, 40]. The source terms in Maxwell's equations for bulk propagation are calculated using the first excitonic resonance (which is sufficient for off-resonant excitation) [27]. This approach allows to reproduce the observed SPM and soliton formation [Fig. 2.4]. In this model the SPM is caused by escape from adiabatic following [27]. The numerical parameters are standard GaAs parameters. Plane waves propagating perpendicularly to the QWs are assumed. The effective propagation length and intensity are coupled parameters in this model that need to be adjusted to achieve a good agreement. Therefore, the effective length has been set to 300 μm and reduced the peak pulse intensities. This necessity can be attributed to the neglect of transverse effects such as a defocusing nonlinearity. The main experimental features are well reproduced by the calculations [Fig. 2.6]. All phase jumps occur as expected, although the SPM beating is less pronounced. The exact temporal variation of the phase depends sensitively on the pulse parameters chosen. The phase evolution in Fig. 2.6(d) and that of the input pulse differ by a linear phase term, i.e., a slight spectral shift. The measured spectra are well reproduced by numerically calculated spectra (not shown here).

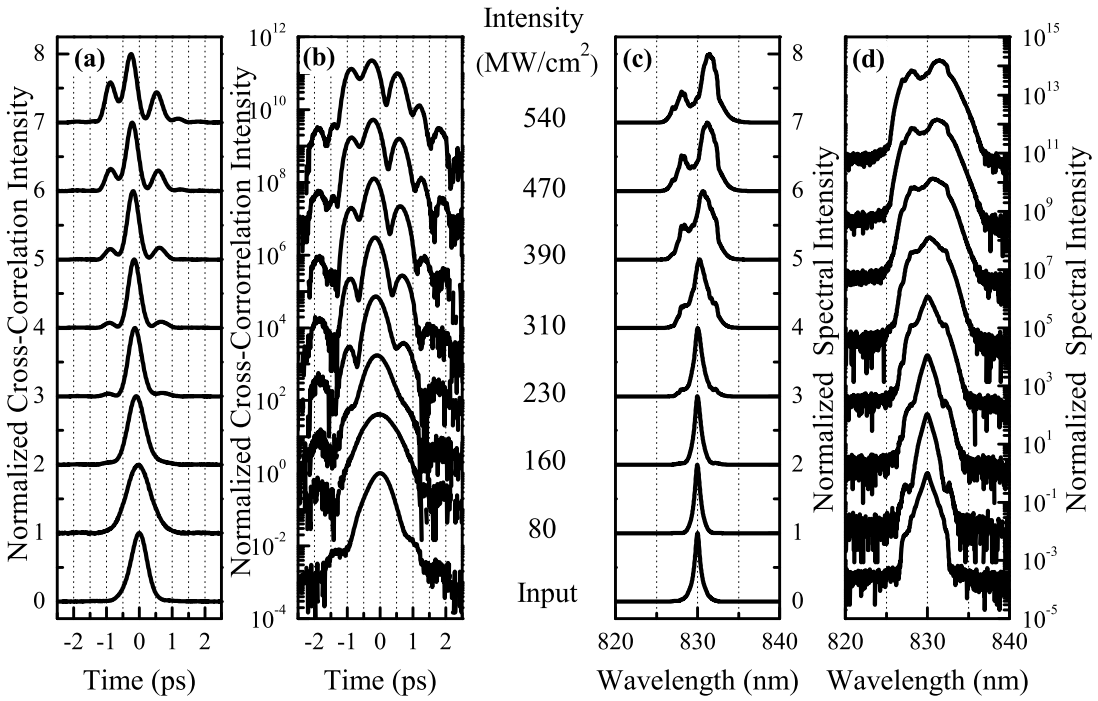

Figure 2.7.: (a),(b) Normalized cross-correlation and (c),(d) spectral intensities for the input pulse at 830 nm (lowest curves) and output pulses after propagation through a 750-μm-thick GaAs sample for different input intensities. (a),(c) Linear and (b),(d) logarithmic scales.

2.4. Pulse propagation in bulk GaAs

2.4.1. Intensity dependence

Figure 2.7 shows the results of intensity-dependent pulse propagation through a 750-μm-thick GaAs sample at $T = 9$ K. The central laser wavelength of 830 nm corresponds to a detuning of 25 meV below the band edge. The temporal cross-correlation signals are depicted in Figs. 2.7(a) and 2.7(b), and the corresponding spectra in Figs. 2.7(c) and 2.7(d) on linear and logarithmic scales. The lowest curves display the profile of the input pulse measured without the sample as reference. For illustration purposes, a time delay as imposed by the sample has been subtracted. At an intensity of 80 MW/cm^2, the output pulse duration is increased from initially 580 fs to 835 fs, while the transmitted spectrum is nearly unchanged. The temporal broadening in this linear excitation regime is

due to the material dispersion. Upon an increase of the input intensity from 80 to 310 MW/cm^2, the temporal pulse width continuously decreases and reaches a value of approximately 415 fs, which is well below the initial pulse duration. Wings occur on both sides of the temporal as well as the spectral peak. Beyond 310 MW/cm^2, the duration of the main pulse remains almost constant and a pulse train evolves from the temporal wings. The shift of the main pulse peak to earlier times by up to 250 fs for increasing intensities indicates a negative nonlinear refractive index n_2. The spectral wings simultaneously grow further apart, while the component at the initial laser wavelength declines. At 540 MW/cm^2, two spectral peaks dominate. In consequence of the underlying GaAs absorption profile (cf. Fig. 2.3), the high-energy peak height is considerably reduced with respect to the low-energy peak. Both peaks are separated by $\Delta\lambda \approx 3.5$ nm. This value corresponds to $\Delta E = 6.3$ meV, yielding a temporal beating period of $\Delta t = 660$ fs. The measured separation between peaks of the temporal pulse train amounts to $\Delta t \approx 670$ fs.

Closely below the band edge of a SC, the refractive index $n(\omega)$ exhibits normal dispersion, i.e., a positive GVD parameter β_2. Furthermore, measurements of the nonlinear refractive index by the z-scan method indicate a negative value of n_2 close to the band edge [41]. Accordingly, mainly the contributions from the quadratic Stark effect and two-photon absorption are the physical reasons for the negative n_2. The combination of a defocusing nonlinearity $n_2 < 0$ with normal material dispersion $\beta_2 > 0$ potentiates the evolution of temporal solitons. The formation of soliton-like pulses in SCs below the band edge has already been hinted at by the demonstration of temporal pulse compression [28, 29]. One can infer that the observed broadening and pulse compression are clear signatures of soliton-like pulse propagation. The temporal sidewings are also well-known from soliton evolution in single-mode fibers [25]. The nonlinearly transmitted pulses is only called "soliton-like" as a pure Kerr nonlinearity does not apply for the situation of near-resonant propagation in a SC. This strict distinction is motivated by the necessity to include the optical polarization dynamics at the fundamental band edge. Early investigations attributed asymmetric reshaping of intense ultrashort pulses energetically below the band edge to escape from adiabatic following [27]. A descriptive illustration of this effect is based on the occurrence of spectral SPM sidebands due to adiabatic following. Polarization mediates the coupling between the spectral components, which results in interference terms.

In the time domain, a temporal pulse train is observed. The spectral sidebands are asymmetrically shaped due to the near-resonant band edge. The temporal beating is also highly asymmetric in consequence of the escape from adiabatic following [27]. Similar beating effects induced by the interplay of dispersion and nonlinearity were first discussed in terms of "modulational instability" [36], which is well established and commonly used in the literature today. Du to the physical origin, it is preferable to denote this effect as "SPM beating".

2.4.2. Dependence on the propagation distance and excitation wavelength

In Fig. 2.8, the profiles of pulses propagated through bulk GaAs samples with thicknesses between 250 and 2000 μm are depicted for intensities from 80 to 540 MW/cm^2 at $T = 9$ K. Again, the lowest traces in all charts present the input pulse as a reference. In Fig. 2.8(a), enhanced chirping due to the normal material dispersion leads to increasing temporal broadening. The corresponding spectra in Fig. 2.8(e) show no noticeable deviation from the input spectrum, giving proof of purely linear propagation. The intensity dependence for a propagation length of 750 μm has already been discussed in detail in the previous section. Pulse compression and formation of an SPM beating was shown. For a considerably lower propagation distance of 250 μm, an even more pronounced temporal pulse compression to about 35% of the input pulse duration occurs at the highest intensity [Fig. 2.8(d)]. The corresponding spectrum in Fig. 2.8(h) displays strong spectral broadening, but no splitting yet. At a much longer propagation distance of 1500 μm, a pronounced spectral splitting and an even more extended temporal SPM beating was found. The individual temporal beat components are also broadened. For the thickest sample (2000 μm), the individual temporal pulse components merge together, which can be attributed to transverse spatial, dispersion, and reabsorption effects from the band edge at long propagation distances [Fig. 2.8(d)]. With increasing propagation length, the power per unit area clearly drops down to a level at which linear these effects again dominate the nonlinear effects such as the SPM beating. The split-off component of the spectrum close to the band edge is starting to vanish at 2000 μm propagation distance due to the stronger absorption .

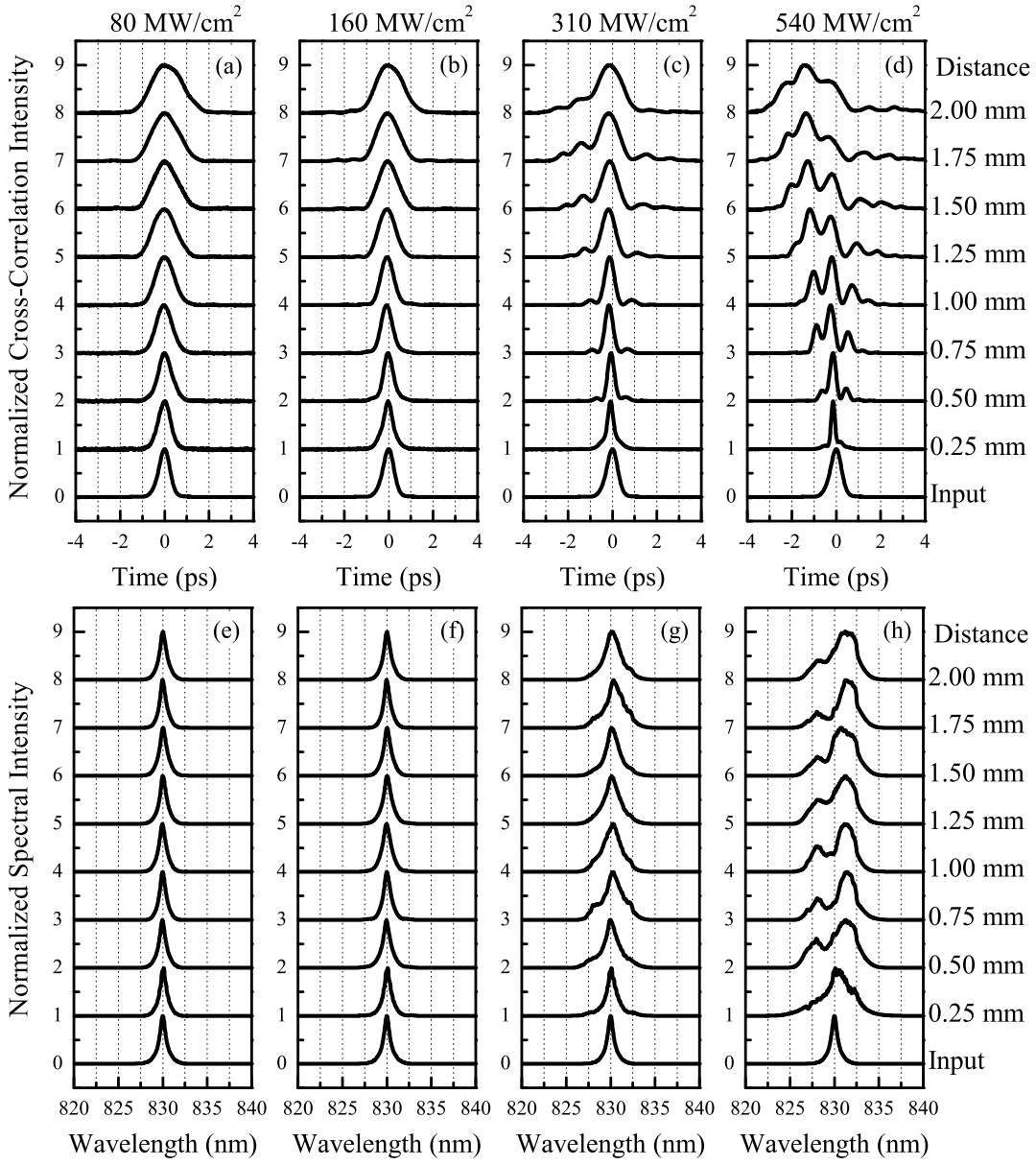

Figure 2.8.: (a)–(d) Normalized cross-correlation signals and (e)–(h) spectral intensities for the input pulse (lowest curves) at 830 nm and transmitted pulses for different propagation distances and input intensities from 80 to 540 MW/cm^2.

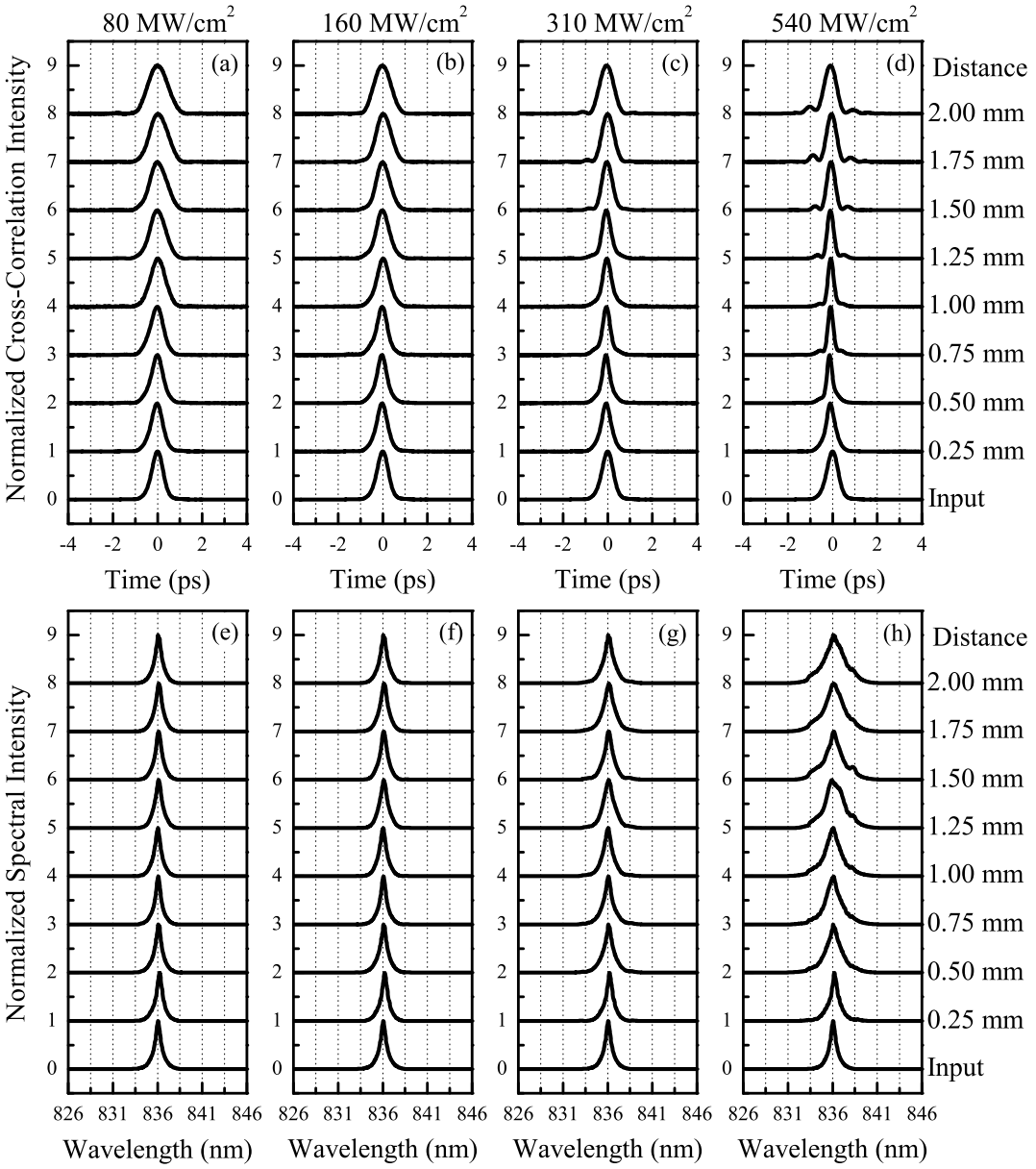

Figure 2.9.: (a)–(d) Normalized cross-correlation signals and (e)–(h) spectral intensities for the input pulse at 836 nm (lowest curves) and transmitted pulses for different propagation distances and input intensities from 80 to 540 MW/cm^2.

Excitation in the proximity of the band edge of a SC implies a strong dispersion of the material parameters. Both, the linear dispersion parameter β_2 and the nonlinear refractive index n_2 are smaller for longer wavelengths. Thus, one can expect a reduction of the nonlinear effects when exciting the sample further below the band edge. The laser was tuned to a wavelength of 836 nm, i.e., about 36 meV below the gap energy of GaAs at $T = 9$ K. Indeed, the dispersive temporal broadening at the lowest intensity is considerably reduced [compare Figs. 2.9(a) and 2.8(a)]. The temporal pulse compression and the SPM beating are also much less pronounced at higher intensities. The spectral splitting even at the highest intensities and longer propagation distances does not occur (see Fig. 2.9(h)). Nevertheless, the development of spectral side wings which causes spectral broadening by almost a factor of three does clearly emerge. The fact that the excitation takes place further away from the band edge (and from the carbon impurity band as well) results in a decreased reabsorption, hence avoiding asymmetries in the spectral and temporal profiles. The smaller absolute value of the coefficient n_2 implicates a smaller influence of SPM on the temporal and spectral pulse profiles.

From the temporal broadening of the lowest-intensity traces for different propagation distances [Figs. 2.8(a) and 2.9(a)], one can infer the GVD parameters β_2 for the two different wavelengths 830 and 836 nm (near and further away from the band edge). The dispersively increased duration of Gaussian pulses depending on the propagation length L can be calculated by [33]

$$\tau_p' = \sqrt{\frac{\tau_p^4 + 16[\ln(2)]^2\beta_2^2 L^2}{\tau_p^2}}\,, \tag{2.39}$$

where τ_p is the duration of the input pulse. One can deduce β_2 to be 0.93 ps^2/cm at 836 nm ($\tau_p = 595$ fs) and 1.63 ps^2/cm at 830 nm ($\tau_p = 580$ fs) from the corresponding fits to the measured pulse widths τ_p' as a function of the propagation distance that are plotted in Fig. 2.10. The strong near-resonant dispersion almost results in a doubling of β_2 by merely tuning the wavelength 6 nm towards the band edge.

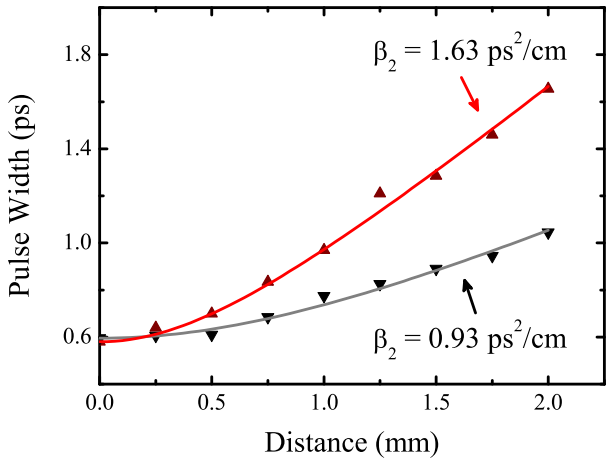

Figure 2.10.: Pulse widths for different propagation distances at an input intensity of 80 MW/cm^2 and wavelengths of 830 nm (upward triangles) and 836 nm (downward triangles). The red and gray curves represent fits based on the temporal broadening of a Gaussian pulse with GVD parameter β_2.

2.4.3. Numerical Simulations

To compare the experimental observations with numerical simulations, the NLSE was solved for the complex electric field envelope A in the following form[2]:

$$\frac{\partial A}{\partial z} = -\frac{\alpha}{2}A - \frac{i}{2}\beta_2\frac{\partial^2}{\partial T^2}A + i\gamma|A|^2A \tag{2.40}$$

with

$$T = t - \beta_1 z. \tag{2.41}$$

using the symmetrized split-step Fourier method as described in Ref. [32]. The NLSE in this form includes dispersion up to the second order, SPM, and damping. The corresponding material parameters are β_2, γ, and α, respectively. The electric field is related to the envelope A by

$$E(t,x,y,z) = Re\left[A(z,t)e^{-\frac{x^2+y^2}{w^2}}e^{-i\omega_0 t}e^{i\beta_0 z}\right] \tag{2.42}$$

with the carrier frequency ω_0 and the transverse pulse width w. The constants β_i $(i = 1, 2, 3)$ are the usual coefficients in the Taylor series expansion of the propagation constant. The pulse is assumed to be Gaussian in transverse space. The

[2]for the derivation refer to section 2.1.1 or Ref. [32]

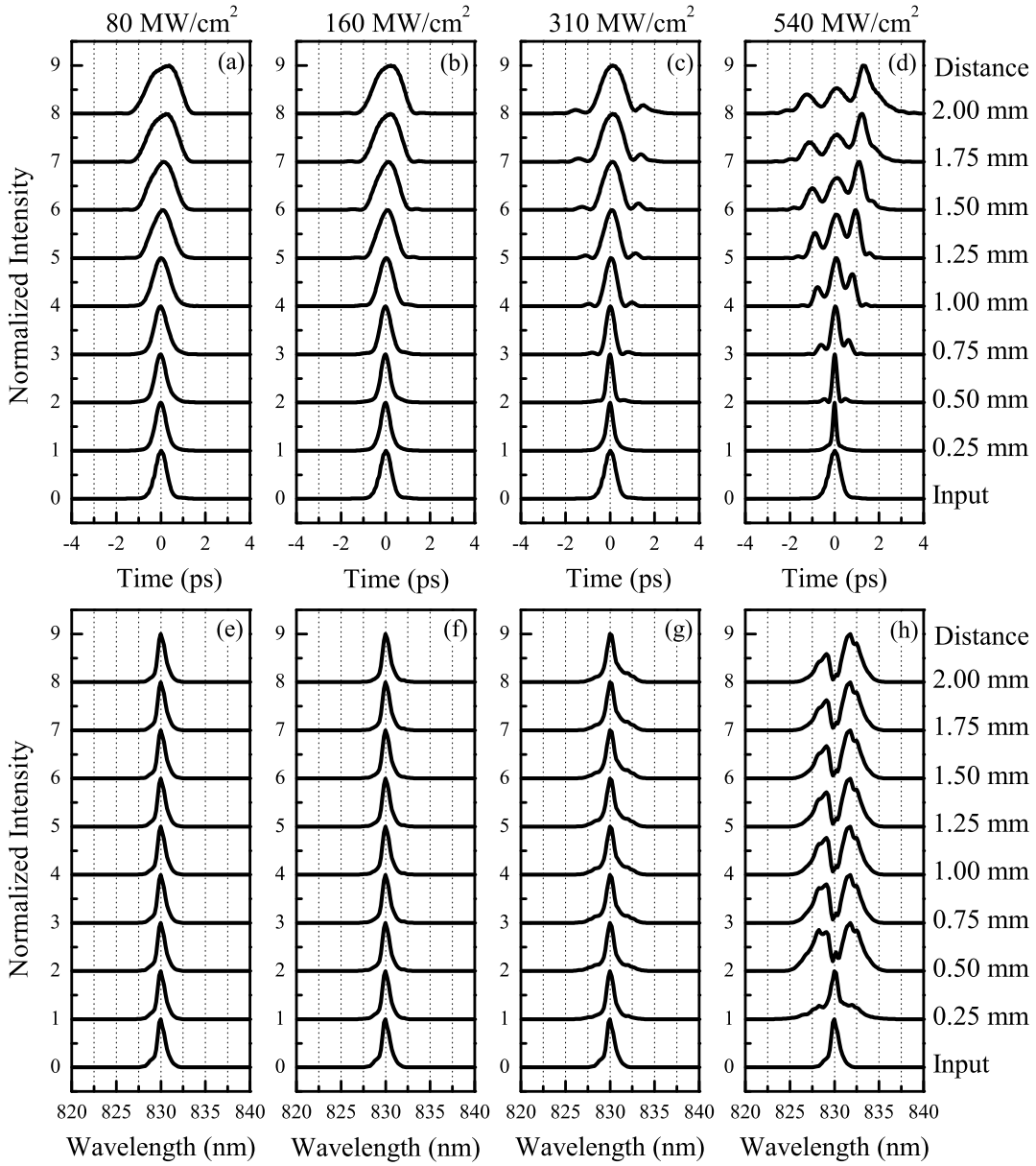

Figure 2.11.: Numerical solutions of the NLSE: (a)–(d) Normalized intensity profiles and (e)–(h) spectra for the input pulse at 830 nm (lowest curves) and transmitted pulses for different propagation distances and input intensities from 80 to 540 MW/cm^2 (the same parameters as in Fig. 2.8).

initial field envelope $A(0,t)$ is taken from the measurements (compare Fig. 2.14). The absolute peak amplitude $A_0 = max_t(|A(0,t)|)$ can be obtained from the measured pulse energy E_{pulse}, the initial transverse pulse width w_0 and temporal pulse duration T_0—assuming a Gaussian shape for both the temporal and spatial dimension—by the formula:

$$A_0 = \sqrt{\frac{\sqrt{32}E_{pulse}}{\pi w_0^2 \epsilon_0 c_0 n \sqrt{\pi} T_0}}. \tag{2.43}$$

Equation (2.40) can be separated into a linear and a nonlinear term

$$\frac{\partial A}{\partial z} = (\hat{D} + \hat{N})A \tag{2.44}$$

with the linear operator

$$\hat{D} = -\frac{\alpha}{2} - \frac{i}{2}\beta_2 \frac{\partial^2}{\partial T^2} \tag{2.45}$$

and the nonlinear operator

$$\hat{N} = i\gamma|A|^2. \tag{2.46}$$

The split-step Fourier method approximates the solution to the NLSE by propagating the optical field over a small distance h where the linear and nonlinear effects are treated independently. Each numerical step is calculated using the formula

$$A(z+h,T) = \exp\left(\frac{h}{2}\hat{D}\right) \exp\left(\int_z^{z+h} \hat{N}(z')dz'\right) \exp\left(\frac{h}{2}\hat{D}\right) A(z,T). \tag{2.47}$$

The expression $\exp\left(h\hat{D}\right)$ is calculated in the Fourier domain by substituting $\frac{\partial}{\partial T} \rightarrow i\omega$ in $\hat{D}$:

$$\exp\left(h\hat{D}\right) B(z,T) = \mathcal{F}^{-1}\left(exp\left[h\hat{D}(\frac{\partial}{\partial T} \rightarrow i\omega)\right] \mathcal{F}(B(z,T))\right) \tag{2.48}$$

where $\mathcal{F}$ and $\mathcal{F}^{-1}$ are the Fourier transform and its inverse, respectively. At this point an experimentally determined frequency-dependent absorption coefficient $\alpha(\omega)$ as shown in Fig. 2.3 is introduced into the equation. To account for the transverse pulse broadening induced by diffraction which doubles the spatial pulse width w after 400 μm of propagation, a constant offset α_{diff} (with $e^{-\alpha_{\text{diff}} \cdot 400\mu m} = \frac{1}{2}$)

is added and then α in the operator $\hat{D}(\omega)$ [equation (2.48)] is replaced by $\alpha(\omega) + \alpha_{\text{diff}} = \alpha(\omega) + \frac{\ln(2)}{400\ \mu m}$. The integral $\int_z^{z+h} \hat{N}(z')dz'$ in Eq. (2.47) is approximated by

$$\int_z^{z+h} \hat{N}(z')dz' \approx \frac{h}{2}[\hat{N}(z) + \hat{N}(z+h)]. \tag{2.49}$$

To calculate $\hat{N}(z+h) = i\gamma|A(z+h)|^2$, the fourth-order Runge-Kutta method is used to determine $A(z+h)$, i.e., to solve the differential equation

$$\frac{\partial A}{\partial z} = i\gamma|A|^2 A. \tag{2.50}$$

The dispersion parameter β_2 is determined experimentally (compare Fig. 2.10) while n_2 or $\gamma = \frac{2\pi n_2}{\lambda}$ is a fit parameter in this model. The simulations revealed that $n_2 = -9.6 \cdot 10^{-19}\ \frac{m^2}{V^2}$ delivers the best results, i.e., the best overall compliance in the temporal and spectral shapes. This value is 3.2 times higher than that reported in Ref. [42] for a wavelength of 1064 nm at room temperature. Since the low-temperature measurements clearly show that n_2 increases considerably from 836 nm to 830 nm (by about a factor of two as described in Sec. 2.4.4) and taking into account the wavelength dependence of n_2 with respect to the gap energy (compare Ref. [41]), the factor of 3.2 is a reasonable assumption.

To perform the calculations described above, a Matlab program was written. The results of the simulations are plotted in Fig. 2.11 for the same parameters as for the cross-correlation measurements in Fig. 2.8. The comparison shows good qualitative agreement, despite the relatively simple NLSE model. The dispersive broadening at low input intensities is reproduced quantitatively [Fig. 2.11(a),(b),(e),(f)]. The spectral broadening and modulations in the temporal wings at 310 MW/cm^2 become clearly visible, however, slightly less distinct when compared to the experimental profiles. At high intensities where nonlinearity plays a dominant role the strong initial pulse compression and the development of an SPM-induced beating with a decreasing modulation frequency due to dispersive pulse broadening occur in the expected way. The calculated spectra qualitatively show exactly the same behavior as those observed experimentally: At 250 μm, the spectrum is considerably broadened but still features only one peak. During the next 250 μm of propagation, the spectrum splits up into two components. Further propagation leads to a decrease of the height ratio between

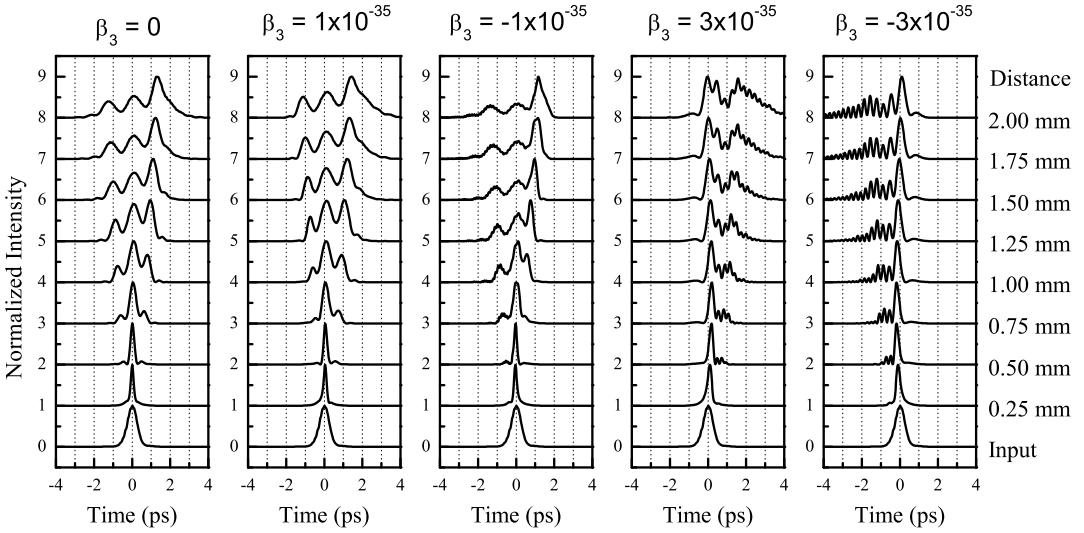

Figure 2.12.: Numerical solutions of the NLSE: (a)–(d) Normalized intensity profiles for the input pulse at 830 nm (lowest curves) and transmitted pulses for different values of β_3 and different propagation distances at an input intensity of 540 MW/cm^2 (the same parameters as in Fig. 2.11(d) except $\beta_3 \neq 0$).

the peak closer to the band edge and the one further away. The development of an SPM-induced beating in the time domain is slightly more pronounced in the measured data. The height ratios of the individual pulse components differ notably between experiment and simulations, especially for longer propagation lengths. These deviations are due to simplifications in the model. First of all, the simulations assume a constant nonlinear refractive index n_2, although a comparison of Figs. 2.8 and 2.9 would suggest a strong frequency dependence. Secondly, all transverse spatial effects that occur due to the defocusing nonlinearity ($n_2 < 0$) have been neglected. A spatially complex pulse also experiences spatial filtering during the sum-frequency generation process of the cross-correlation which the calculations cannot account for. Furthermore, dephasing effects and deviations from a pure Kerr nonlinearity (cf. Sec. 2.4.1) are not modeled by the NLSE. Considering these simplifications, the agreement between experiment and simulations is still remarkably good, assuring that all relevant contributions are included in the model. This identifies pulse propagation in the considered regime to be dominated by the frequency-dependent absorption profile, second order dispersion and defocusing Kerr nonlinearity.

To determine whether third order dispersion (i.e. $\beta_3 \neq 0$) plays a significant role, simulations using the same parameters as in Fig. 2.11(d) where performed with a range of values for β_3. The results are depicted in Fig. 2.12. Values up to $\pm 10^{-35}$ show very little deviation from the $\beta_3 = 0$ case except for a slight steepening at the rising edge (positive β_3) or the falling edge (negative β_3), respectively. For $\beta_3 = -1 \times 10^{-35}$, the first indications of a high frequency modulation of the pulse envelope are visible. Increasing the third order dispersion parameter by a factor of 3 leads to a strong increase of these modulations. Depending on the sign, they appear at the front of the back side of the pulse. Further increase of β_3 results in a complete pulse distortion (not shown). Since neither very steep edges nor any such high frequency modulations have been observed in the experiments, a strong influence of third order dispersion can be safely ruled out. For this reason, β_3 was set to zero in all simulations shown above.

2.4.4. Temporal phase evolution

To obtain additional insight into the temporal and spectral behavior, XFROG traces [Fig. 2.13] for the propagation of 600 fs pulses through a sample of the optically polished 600-μm-thick GaAs wafer have been measured. At an input pulse wavelength of 830 nm, the intensity was continuously varied from 10 to 580 MW/cm^2.

Figures 2.14 and 2.15 show the results retrieved by the XFROG algorithm. In Fig. 2.14, the red and black lines represent the phase and the normalized intensity versus time, respectively. Please note the different phase scales in Figs. 2.14(e) and 2.14(f) compared to those in Figs. 2.14(a)–(d). The corresponding normalized spectral intensities are displayed in Fig. 2.15. The input pulse shown in Fig. 2.14(a) exhibits a nearly constant phase over the pulse with slightly chirped outer wings. Linear propagation at an input intensity of 10 MW/cm^2 leads to a parabolic phase with negative curvature. According to the sign conventions, this represents a positive linear chirp which is due to the normal material dispersion. The pulse duration is therefore considerably increased. The unaltered spectrum with respect to the incident spectral profile gives proof of the linear propagation [compare Figs. 2.15(a) and 2.15(b)]. At 160 MW/cm^2 [Fig. 2.14(c)], the phase curvature is reversed and the pulse duration has decreased below that of the input pulse. This is a consequence of incipient SPM. It also results in a spectrum that features slight wings, i.e., a first indication of spectral broadening [Fig. 2.15(c)]. These features are much more pronounced at an elevated input intensity of 270 MW/cm^2 [Fig. 2.14(d)]. The main pulse is further compressed with small wings arising on both sides of the peak. Steep phase jumps of approximately 0.75 π separate the temporal pulse components. Such behavior is well known from the soliton evolution over several meters of optical fiber at a wavelength $\lambda_0 = 1.55$ μm and corresponds to an excitation slightly above the fundamental temporal soliton order $N_t = 1$ [25]. In this case, however, n_2 and β_2 exhibit reversed signs. Upon further increase of the input intensity up to 580 MW/cm^2 [Fig. 2.14(e) and 2.14(f)], the SPM beating as introduced above forms an asymmetric temporal pulse train. Phase jumps of almost π occur between the pulse components and provide clear signatures of a beating phenomenon (compare the linear beating phenomena observed on resonance in Ref. [24] and Fig. 2.4). In the spectral domain, increase of the intensity from 270 to 580 MW/cm^2 [Figs. 2.15(d)–

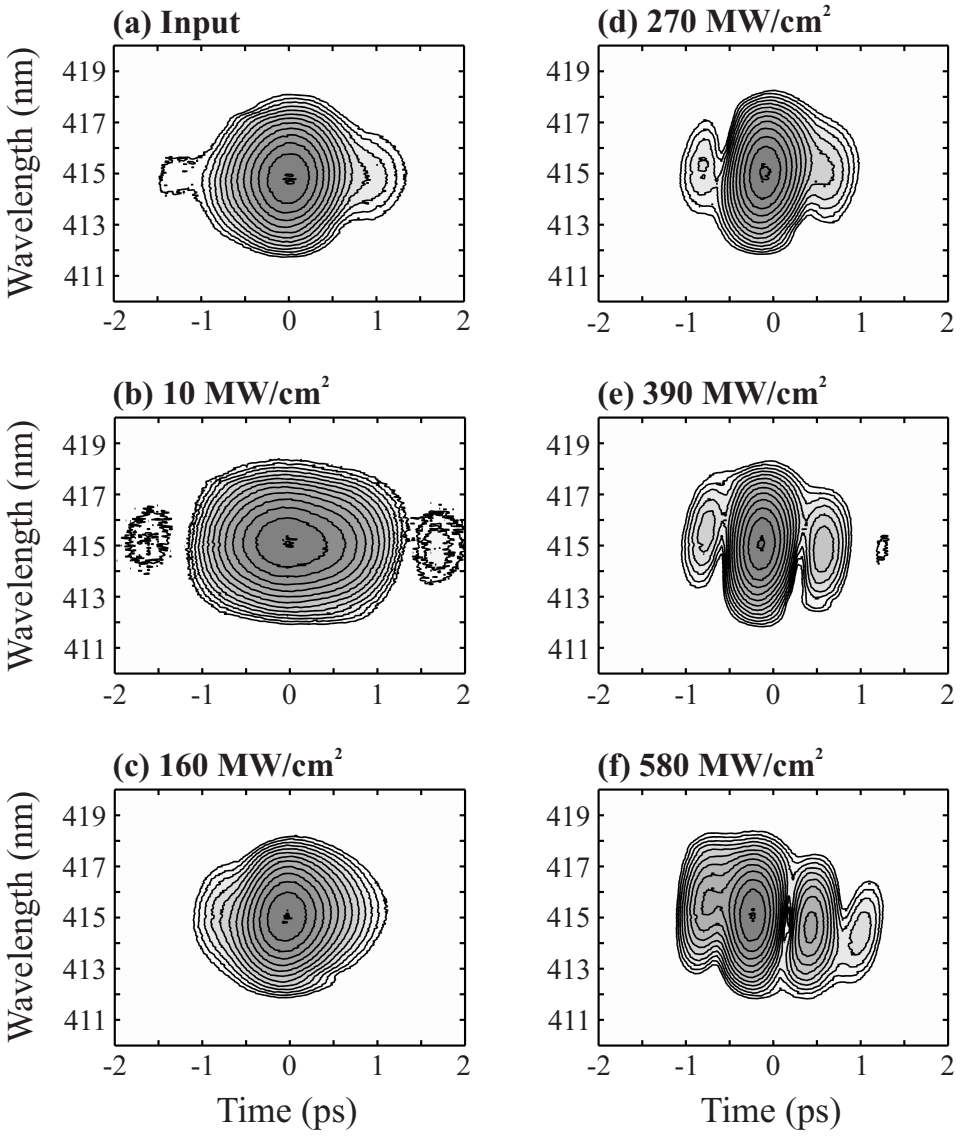

Figure 2.13.: XFROG traces for (a) the input pulse at 830 nm and (b)–(f) after propagation through an optically polished 600-μm-thick GaAs wafer at $T = 9$ K for input intensities from 10 to 580 MW/cm^2. The contour lines range from 95% to 0.5% of the peak intensity and represent an increase/decrease of the intensity by a factor of 1.5 with respect to each other.

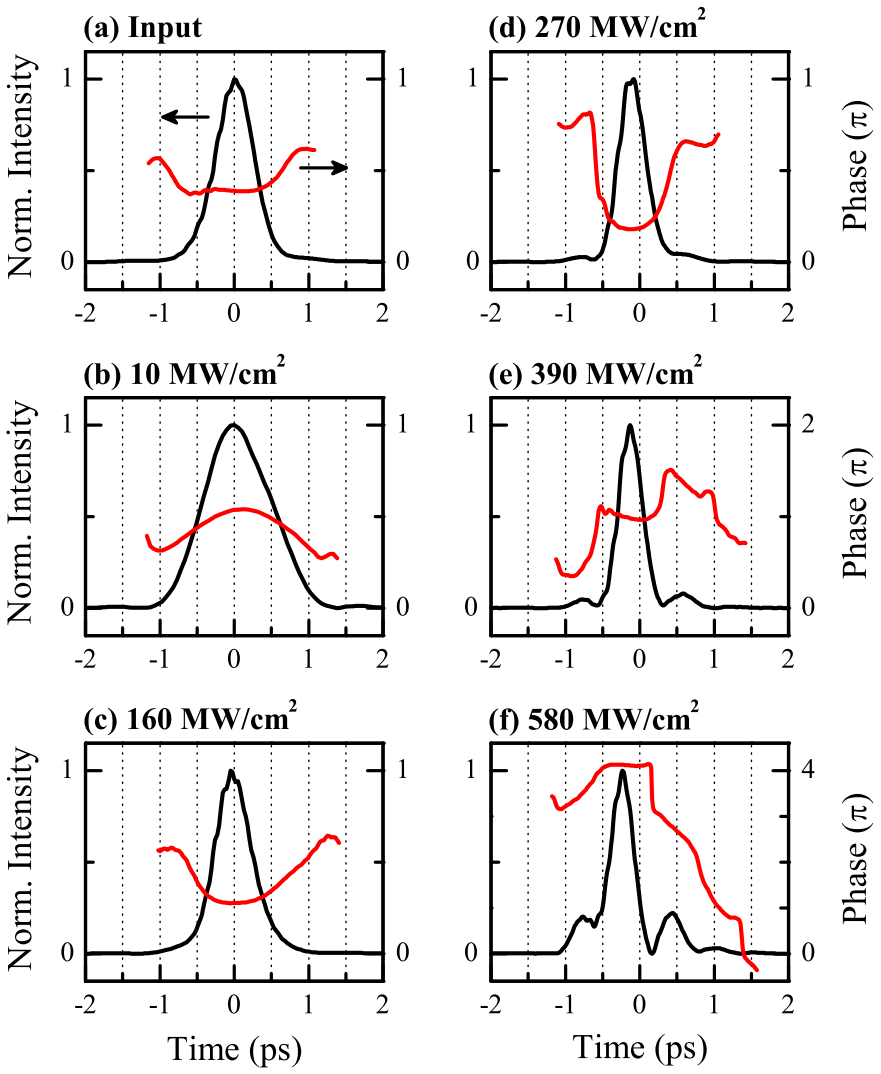

Figure 2.14.: Normalized retrieved intensities (black lines) and phases (red lines) versus time for (a) the input pulse at 830 nm and (b)–(f) after propagation through an optically polished 600-μm-thick GaAs wafer at $T = 9$ K for input intensities from 10 to 580 MW/cm^2.

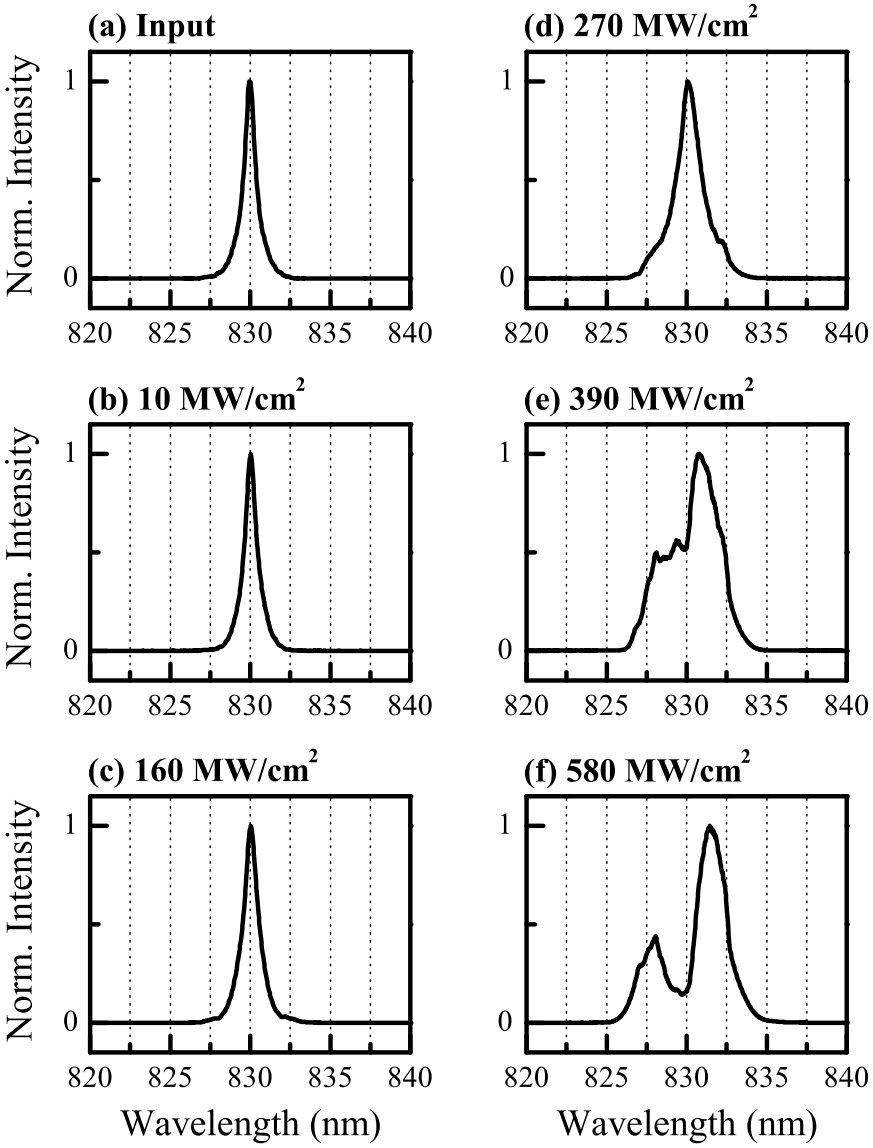

Figure 2.15.: Normalized retrieved spectra for (a) the input pulse at 830 nm and (b)–(f) after propagation through an optically polished 600-μm-thick GaAs wafer at $T = 9$ K for input intensities from 10 to 580 MW/cm^2.

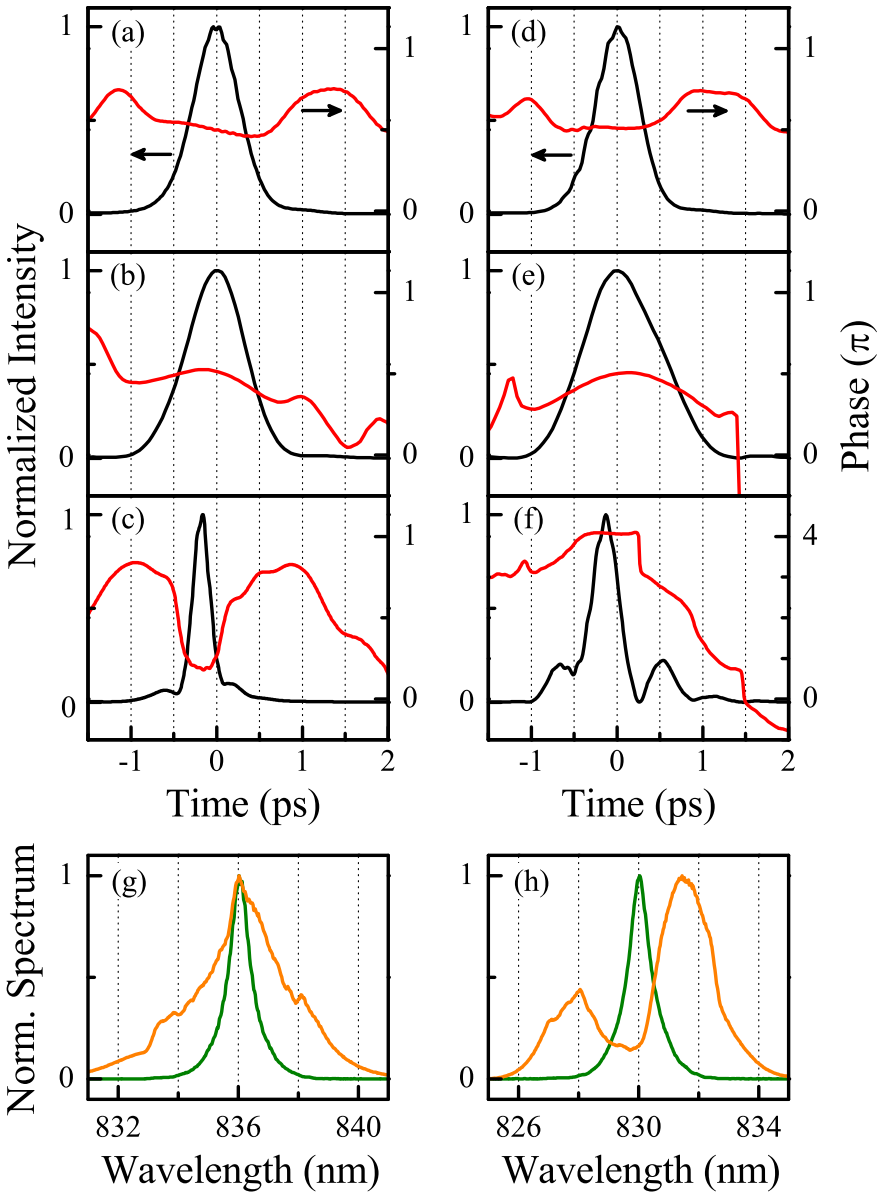

Figure 2.16.: (a)-(f): Normalized retrieved intensities (black lines) and phases (red lines) versus time for the 600 fs input pulse [(a) and (d)] and after linear propagation at 8 MW/cm^2 [(b) and (e)] and nonlinear propagation at 580 MW/cm^2 [(c) and (f)] through 600 μm of bulk GaAs. (g) and (h): Normalized measured spectra after linear propagation of 600 fs input pulses at 8 MW/cm^2 (green lines) and nonlinear propagation at 580 MW/cm^2 (orange lines) through 600 μm of bulk GaAs. Left side: input pulse at 836 nm. Right side: input pulse at 830 nm.

(f)] leads to spectral wings that grow at the expense of the initial spectral profile. At the highest measured intensity of 580 MW/cm^2, the spectrum is split into two distinct peaks. The intensity of the component closer to the band edge is again lower due to band-edge reabsorption. The initial laser spectrum is strongly suppressed by the SPM, i.e., converted into newly developed frequency components. The phase behavior becomes more complicated with increasing intensity due to the interplay of dispersion and nonlinearity. The main temporal peak develops a constant phase, indicating soliton-like propagation in terms of a balance between the defocusing nonlinearity and the normal material dispersion. The adjacent pulse components start to develop a linear phase, but with different slopes, i.e., different carrier frequencies. The outer pulse components show a positive phase curvature which reflects SPM. The temporal delay and spectral shift of the individual pulse components however must be attributed to the material dispersion. This is especially evident in the gradual merging of the precursor and the main pulse which prevents a clear phase jump in between. A comparison of the XFROG traces in Figs. 2.13(b) and 2.13(f) demonstrates this behavior: The traces are both sloped downwards, while the trace of the single soliton-like compressed pulse [Fig. 2.13(c)] is tilted upwards as expected for dominant SPM. Furthermore, the phase jumps around the main pulse eventually revert their directions. Whereas steep phase jumps of $\pm\pi$ are almost equivalent, the direction still reflects underlying frequency shifts.

In the following, the focus is placed on the influence of the detuning between laser spectrum and band edge. Figure 2.16 illustrates the retrieved temporal intensity and phase profiles of the input [Fig. 2.16(a) and (d)], the linearly [Fig. 2.16(b) and (e)] and the nonlinearly propagated pulses [Fig. 2.16(c) and (f)] with equal input intensities for the two wavelengths $\lambda_0 = 836$ nm and 830 nm, respectively. In both cases, the input pulse envelope [black lines in Fig. 2.16(a) and (d)] features a duration of about 600 fs. The corresponding phases [red lines in Fig. 2.16(a) and (d)] are both nearly constant during the pulses, exhibiting only slight chirp at the outer wings. The XFROG trace in Fig. 2.13(a) shows though, that these wings are only of the order of 1% of the peak intensity. Comparison of the intensity and phase profiles for linear propagation at 8 MW/cm^2 [Fig. 2.16(b) and (e)] immediately reveals the large dispersion of the GVD parameter β_2 at the SC band edge. The phase curvature is considerably enhanced in the case of $\lambda_0 = 830$ nm, yielding a stronger linear dispersion of the material and increased

broadening of the pulse envelope. The lowest curves in Fig. 2.16(c) and (f) (input intensity 580 MW/cm^2) similarly demonstrate a much more pronounced nonlinearity n_2 for an excitation closer to the band edge. Whereas the temporal pulse train is already well-developed with phase jumps of π and considerable dispersive contributions to the pulse wings in case of $\lambda_0 = 830$ nm, the pulse at $\lambda_0 = 836$ nm evolved only to a stage slightly above the soliton order $N_t = 1$. The displayed soliton-like pulse compression is comparable with the effect occurring at 830 nm for an intensity of merely 270 MW/cm^2 [Fig. 2.14(d)]. For a Kerr nonlinear phase shift $\Delta\Phi \propto n_2 I_0$ with the pulse peak intensity I_0, one can therefore roughly estimate an absolute value of n_2 which is reduced by a factor of two when tuning the laser from 830 to 836 nm.

The directly measured fundamental spectra for $\lambda_0 = 836$ nm and 830 nm are plotted in Figs. 2.16(g) and 2.16(h), respectively. The green lines represent the linear spectra measured at an intensity of 8 MW/cm^2, which are identical to the corresponding input pulse spectra. At an intensity of 580 MW/cm^2 and $\lambda_0 = 836$ nm [orange line in Fig. 2.16(g)], the spectrum is rather symmetrically broadened around the input spectrum by the influence of SPM. Yet, the spectral broadening is more pronounced than expected from the spectrum of the 270 MW/cm^2 pulse at 830 nm [compare Fig. 2.15(d)]. In case of the high-intensity propagation at 830 nm, the measured spectrum [orange line in Fig. 2.16(h)] reflects the asymmetric splitting into two distinct spectral wings as already observed in the XFROG retrieval in Fig. 2.15(f). Generally, the directly measured spectra of Fig. 2.16(g) and (h) affirm the high quality and reproducibility even in details of the XFROG retrievals and, hence, of the phase dynamics presented here.

2.4.5. Focusing effects

The samples exhibit a thickness which is considerably larger than the Rayleigh length of the beam waist. Furthermore, a defocusing nonlinearity does not provide self-guiding of the beam. One consequently expects a strong dependence of the pulse evolution on the focusing conditions into the sample. Figure 2.17 shows the corresponding temporal and spectral data for different sample z positions with respect to the position of the beam waist. Here, a negative sign of the z position denotes a sample displacement towards the objective lens (usual z-scan

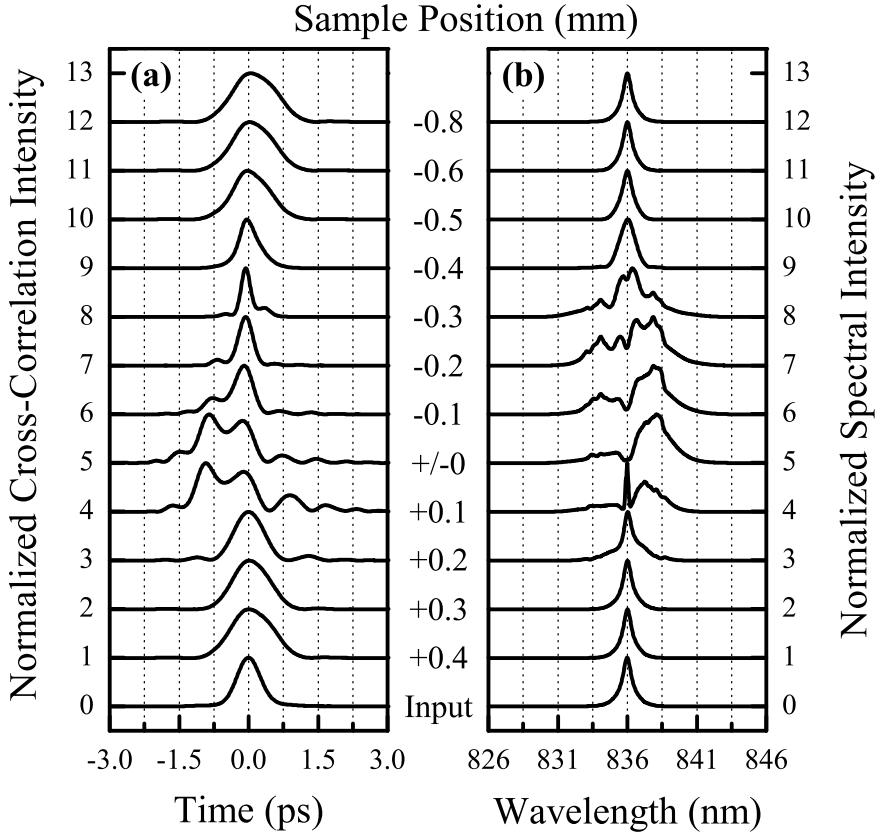

Figure 2.17.: (a) Normalized cross-correlation signals and (b) spectral intensities for the input pulse at 836 nm (lowest curves) and after propagation through a 2-mm-thick GaAs sample at 970 MW/cm^2 for different positions of the sample front surface relative to the focal point of the microscope objective. A negative sign of the position indicates a displacement towards the microscope objective.

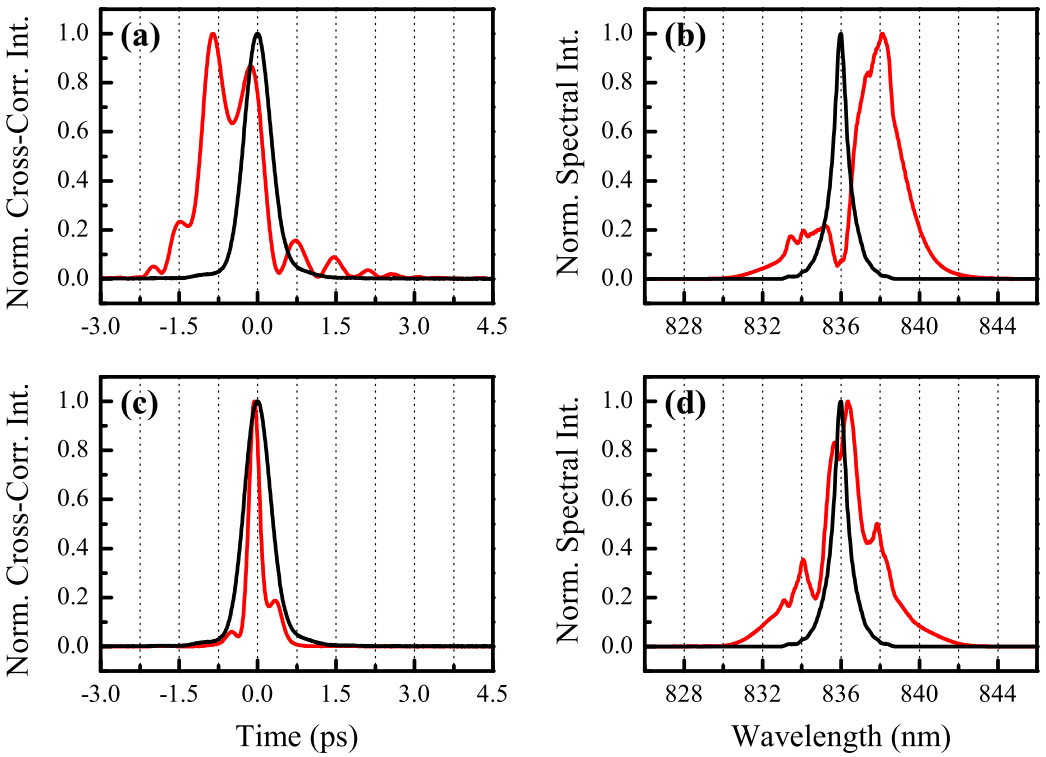

Figure 2.18.: (a),(c) Normalized cross-correlation signals and (b),(d) spectral intensities for the input pulse at 836 nm (black lines) and after propagation at 970 MW/cm^2 through a 2-mm-thick GaAs sample (red lines). (a),(b) Position of the front surface at the focal point and (c),(d) displaced by -0.3 mm (closer to the microscope objective).

convention). A GaAs sample of 2000 μm thickness and a constant input intensity of 970 MW/cm^2 at wavelength $\lambda_0 = 836$ nm have been used. A z position of zero corresponds to the temporal traces and spectra that have been discussed in the previous sections. In this case, the spectral splitting due to SPM along with the asymmetric temporal SPM beating was observed. At $z = -0.3$ mm, i.e., after moving the focus into the sample, temporal pulse compression by a factor of two by nonlinear propagation through 2000 μm of bulk GaAs is evident. In this case, the spectrum does not exhibit the already observed splitting into two parts, but yields a rather symmetric profile typical of Kerr solitons [36]. Considering the temporal dynamics discussed in Sec. 2.4.4 based on the XFROG measurements, one can call this case "dominantly soliton-like", whereas the situation at $z = 0$ mm (SPM beating) is called "dispersively influenced". Both cases are presented in detail in Fig. 2.18. In these plots, the black lines illustrate the input pulse profile as a reference. For larger sample displacements in either direction in Fig. 2.17, a linear propagation behavior is recovered.

The defocusing nonlinearity is responsible for the difference between both situations depicted in Fig. 2.18. In the case of $z = 0$ mm, the maximum intensity is reached at the sample surface. This results in maximum SPM and nonlinear phase shift, i.e., maximum spectral splitting. On the other hand, nonlinear diffraction due to defocusing nonlinearity leads to a rapid decay of the intensity during propagation. Hence, the SPM beating and the "dispersive wings" are subject to the linear material dispersion. These assumptions are confirmed by Fig. 2.8(h): The nonlinear phase shift in SPM depends on intensity *and* propagation distance. Initially when entering a long sample, i.e., for low propagation distances, the spectrum broadens and splits into two major parts. After a certain effective nonlinear propagation length, which is about 1 mm for $z = 0$ mm (focus on the surface), the spectral SPM splitting does not increase any more and subsequently washes out. Figure 2.8(d) demonstrates that the linear dispersive contributions to the temporal pulse evolution are dominant beyond this effective length. This is the obvious situation in Figs. 2.18(a) and 2.18(b). In the case of $z = -0.3$ mm, the waist is mainly lying within the bulk sample. Hence, the Gaussian beam radius $w(z)$ does not vary as much during propagation. This implies that the dispersion may be effectively (over-)compensated by SPM. Therefore, the propagation is dominantly soliton-like [compare Figs. 2.18(c) and 2.18(d)].

2.5. Conclusions and outlook

This comprehensive study of pulse propagation in SC MQW Bragg structures (1D resonant PCs) at low temperature has shown that diverse light-matter interaction phenomena occur, each dominant in a certain intensity range. A fast-scanning XFROG technique was applied to resolve the temporal amplitude and phase dynamics of propagating pulses for intensities from the linear to the highly nonlinear regime. Based on the results from the phase-resolved measurements and the numerical simulations presented in this chapter, it was possible to clearly identify the effects in the different intensity regimes and the transitions between them. This includes linear propagation, breakdown of the PBG, self-induced transmission, as well as an SPM-induced beating at the highest applied intensities.

To separate the influence of the bulk part of the structure from the that of the QWs, near-resonant propagation in bulk GaAs has been studied. The dependence on the input intensity, the sample length, and the excitation wavelength have been covered. In the time domain, the observations included a pronounced pulse compression by more than a factor of two and the formation of a pulse train including a soliton-like main pulse, which arises from the interplay of the normal material dispersion and the defocusing nonlinearity energetically below the GaAs band edge. A longer sample results in more beating periods and considerable pulse broadening. The strong dispersion of the linear and the nonlinear refractive index leads to different pulse characteristics when tuning the wavelength away from the band gap by only 6 nm. Numerical simulations based on the NLSE identified the absorption profile, normal second order dispersion, and defocusing Kerr nonlinearity to be the dominating effects. The phase-resolved measurements allowed for studying the interplay of dispersion and SPM in great detail. Based on these results, the effects observed in the MQW Bragg structure can be clearly separated: In the linear regime, the PBG generated by the superradiant mode of the QWs totally dominates the interaction between the propagating light pulses and the structure. The observed self-induced transmission after the PBG breaks down at an intermediate input intensity must also be attributed to the carrier dynamics in the nonlinearly excited QWs as it is not present in the results measured with the bulk samples. However, the SPM occurring at high intensities is evidently caused by the bulk part of the structure. In this regime, the influence of

the QWs is so small that it can only be discerned by looking at the phase changes of the propagated pulses.

The studies presented here constitute a large contribution to the understanding of sub-picosecond phenomena in SC MQW Bragg structures and bulk SCs. Together with previous publications on SC MQW Bragg structures [5, 6, 9], very few questions are left open. Applications using nonlinear effects of periodically spaced QWs are limited by the relatively low breakdown threshold of the PBG and the strong SPM occurring in the inevitable[3] bulk substrate. A solution for providing an intensity stable PBG combined with the collective QW dynamics may be the so-called resonantly absorbing Bragg reflectors (RABRs) [43–45]. Such structures consist of alternating layers with different refractive indices and periodically embedded QWs. This gives them the unique property of a resonance that is degenerate or nearly resonant with the Bragg frequency. They are promising with respect to supporting gap solitons. RABRs are subject to ongoing, mostly theoretical research [46], but so far no experimental observation of gap solitons is known. The main reason is surely that such structures are very challenging to fabricate [47].

Apart from giving new insight into the fundamentals of light interaction with SCs, the studies on bulk GaAs also confirm that it should be possible to directly produce short optical pulses from a SC laser diode as suggested in Ref. [28] by exploiting the observed pulse compression effect. The results are particularly useful since GaAs is one of the most important materials used in the design of laser diodes.

[3]Since high-quality MQW ensembles without a substrate will very likely lack mechanical stability, the only possibility to to avoid the bulk effects would be to find another substrate material with very low nonlinearity and the same lattice structure (to prevent strain) as GaAs at the same time. This is believed to be a currently insuperable technical challenge.

Chapter 3
Nonlinear transmission dynamics of metal-dielectric photonic crystals

In this chapter, the nonlinear optical properties and dynamics of one-dimensional metal-dielectric photonic crystals (1DMDPCs) are discussed. The structures in question are stacks of periodically spaced thin (a few nanometers) metal films separated by a dielectric material. Previous publications predict a high potential of these structures for applications such as ultrafast all-optical switching due to a strongly nonlinear relation between the material's transmission and the incident light field intensity. The demand in telecommunication and integrated optics for new concepts to design all-optical packet switching devices with sub-picosecond switching time is very high.

To my knowledge, the presented measurements constitute the first time-resolved studies on the nonlinear transmission of 1DMDPCs that have been published so far, and thus rightfully can be called pioneering experiments. Several theoretical investigations on this subject have been published [12–15], as well as a few experimental results [11, 16, 17], but none of them deals with the temporal dynamics. The main results of this chapter have been presented in a post-deadline talk at the *Frontiers in Optics 2007* conference in San Jose (USA).

This chapter is structured as follows: First, the concept and the current state of the research in this field are outlined. This is followed by an introduction to the dynamics in metal nano-structures if they are excited by a laser pulse. Subsequently, the sample fabrication method and the experimental setup

are described. Then the results from time-resolved transmission measurements, primarily sub-picosecond resolution pump-probe experiments, are shown and the identified nonlinear effects are discussed. Finally, conclusions are drawn from the observations and an outlook for further investigations in this field of research is given.

3.1. The current state of research

1DMDPCs, i.e., arrangements of periodically alternating layers of a metallic and a dielectric material such that the complex index of refraction periodically alternates between two values, are commonly used as Bragg reflectors since they form a wide photonic band gap. However, such a structure also remains transparent in certain spectral regions even if the accumulated thickness of the metal layers is increased to multiples of the skin depth in bulk metal [48, 49]. This unique feature allows for exploiting the nonlinear transmissive properties of metals which are often neglected due to the high reflectivity [13]. A strong nonlinearity means that it is possible to drastically change the structure's optical properties using a strong light field, usually an intense ultrashort laser pulse. The experiments in this work concentrate on the transmissive properties and their role in possible applications although nonlinear changes of the reflectivity are to be expected as well.

Recent experiments [11] using the well-known open-aperture z-scan technique [50] report a nonlinear transmission decrease by a factor of 2.5 if the material is pumped by a laser with an intensity of 500 MW/cm^2 at the focus spot. Numerical calculations [15] predict the possibility to achieve a linear transmission of more than 60% in 1DMDPCs that can be suppressed to below 5% using intense laser pumping with a peak intensity of 15 GW/cm^2. Thus, these structures are very promising for the development of an ultrafast all-optical switch, i.e., a device that can be transferred from a highly transmissive into a dominantly reflective or absorptive state by an ultrashort laser pulse. This mechanism could for example be used in optical data transmission to selectively block temporal sections of a digital signal, i.e., for applications such as multiplexing and demultiplexing.

Usually, the optical nonlinearity in noble metals is attributed to the Fermi smearing mechanism [51], i.e., the modification of the Fermi distribution of the conduction electrons which are heated up by intense laser pulses. Fermi smearing has a sub-ps response time and its relaxation time is typically on the order of 1 ps. Using a structure as described above should considerably enhance the nonlinear response due to the high amount of metal in the light path while maintaining the fast reaction times. However, this assumption has not been verified yet since no time-resolved measurements of the nonlinear transmission have been published

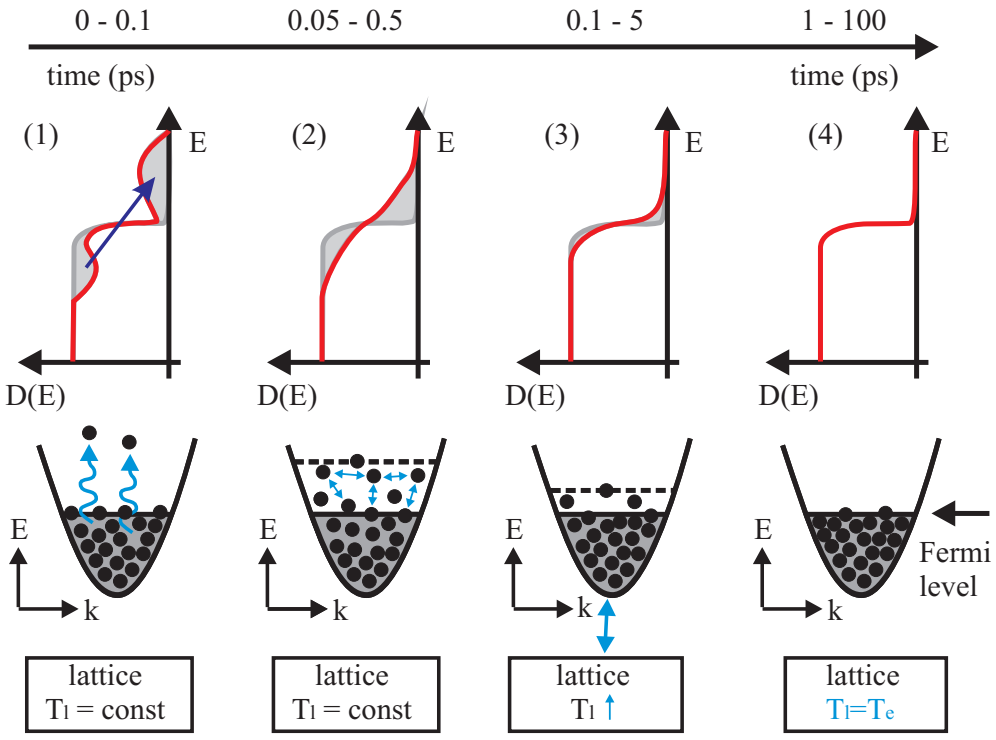

Figure 3.1.: The four phases of the dynamics in metal particles or thin films after excitation by a strong laser pulse. Phases (1)-(3) show the Fermi smearing.

up to now.

The goal of the work described in this chapter was to study the temporal dynamics of the strong nonlinear transmission changes in 1DMDPCs. Therefore, 1DMDPCs out of silver and silicon dioxide have been manufactured and investigated by pump-probe spectroscopy as described in the following sections.

3.2. Theoretical background

Noble metals are known for their strong nonlinear properties. Studies on gold nano-particles and thin films have shown the possibility to considerably influence their dielectric function ϵ and thereby transmission and reflection by laser excitation. The main reason for changes in ϵ is an increase of the electron gas temperature which can rise by several hundreds of Kelvins in a few femtoseconds.

The dynamics in a metal particle or thin film can be divided into four (overlapping) phases [52–54] on different time scales as depicted in Fig. 3.1:

(1) Excitation of the electron gas: Photons from the pump pulse are absorbed by electrons. In the experiments shown here the photon energy of the pump light is below the energy needed for interband transitions (which are at 3.99 eV/310 nm and 3.95 eV/322 nm for silver [52]), thus the electrons are predominantly excited via intraband transitions and surface plasmons, which have a dephasing time of less than 100 fs. Directly after the excitation, the electrons have a non-Fermi-Dirac (or non-thermal) energy distribution, i.e., there are some hot electrons energetically far above the Fermi level, but the majority of the electron gas is left cold. Therefore, the initial change of the dielectric function ϵ is relatively weak.

(2) Thermalization of the electron gas: Within several tens to a few hundreds of femtoseconds, the excited electrons equilibrate with the remaining free electrons by electron-electron scattering. The electron energies reach a Fermi-Dirac distribution corresponding to a temperature that can easily reach several hundred Kelvins above the initial temperature. At this point the magnitude of the ϵ change is the highest. The lattice however still remains cold, i.e., at the temperature before the laser excitation, and is therefore far from thermal equilibrium with the strongly heated electron gas.

(3) Equilibration of the electron gas with the lattice: The free electrons transfer most of their energy to the lattice via electron-phonon interaction. The electron temperature decreases and ϵ tends towards its former value as the heat capacity of the lattice is much larger than that of the electron gas. When electron gas and lattice reach the mutual thermal equilibrium, typically within a time frame of 1 to 5 picoseconds, the common temperature is only a few Kelvins higher than before the excitation. Thus, the effect of a modified ϵ becomes negligible.

(4) Heat diffusion: The excited region of the sample is cooled down by heat transfer to the surrounding temperature bath. The rate of this process depends on the size of the excited volume and the heat conductivity. It is orders of magnitude slower than the previous three steps though.

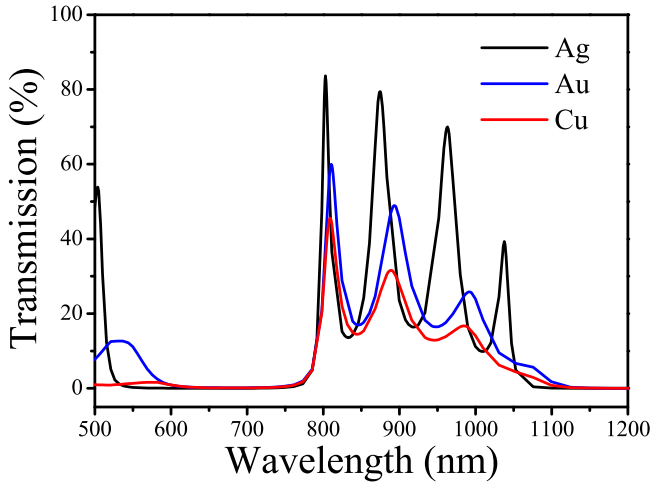

Figure 3.2.: Numerically calculated linear transmission spectra of a 1DMDPC consisting of 5 layers (16 nm each) of silver (black line), gold (blue line), or copper (red line) separated by 250 nm SiO_2.

The thermalization of the electron gas with the lattice, which is the most important process for the recovery time of the pumping-induced transmission change, is usually described as two thermodynamic baths coupled by electron-phonon interaction. The dynamics is commonly described by the two temperature model [55]:

$$c_e(T_e)\frac{\partial T_e}{\partial t} = \chi \Delta T_e - \alpha(T_e - T_l) + f(\mathbf{r}, t) \tag{3.1}$$

$$c_l \frac{\partial T_l}{\partial t} = \alpha(T_e - T_l), \tag{3.2}$$

where T: temperature, c: specific heat, α: electron-phonon coupling constant, χ: thermal conductivity of the electrons, and f stands for the electron heating by the pump photons. The subscripts e and l denote electron gas and lattice, respectively. In this model, the electron gas temperature is governed by three processes represented by the three terms on the right hand side of Eq. 3.1: Heat transport, electron-phonon coupling, and energy intake from laser pumping. The lattice temperature is purely influenced by electron-phonon coupling.

Before starting the sample preparation, linear transmission spectra where calculated using the scattering matrix formalism [56] using experimental values for the dielectric function of the metal as published in Ref. [57]. They are depicted in Fig. 3.2 for three different noble metals. For the experiments, we chose silver and silicon dioxide as materials. Silver exhibits the largest degree of linear transmission compared to most other noble metals [Fig. 3.2]. A field distribution for a silver based 1DMDPC at the wavelength of the maximum transmission is

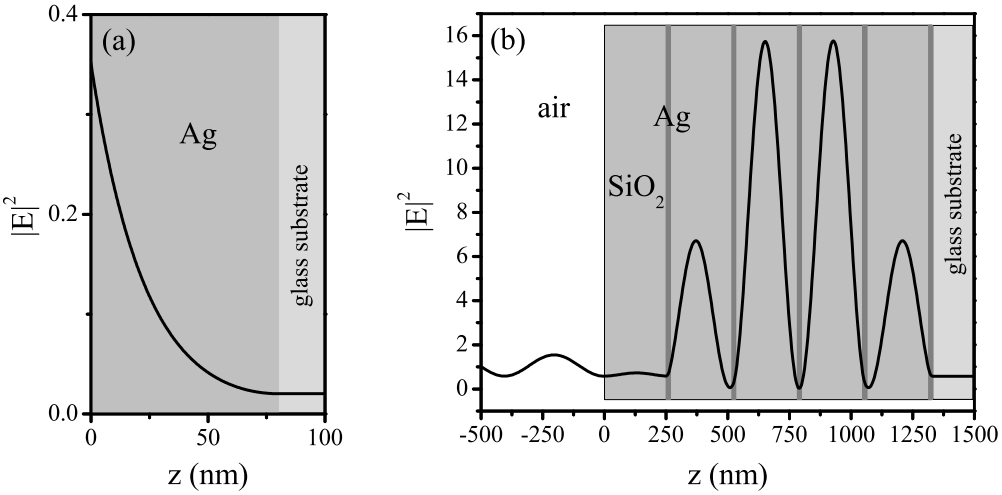

Figure 3.3.: Field distribution calculated using the scattering matrix method [56] in (a) one 80 nm silver film and (b) a 1DMDPC consisting of 5 layers of 16 nm silver each separated by 250 nm SiO_2. The filed distribution is normalized to the incident field.

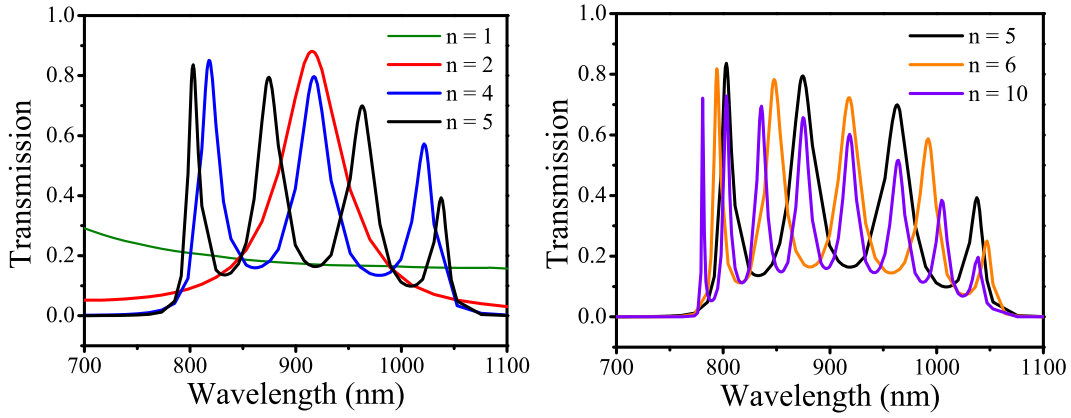

Figure 3.4.: Numerically calculated transmission spectra for different numbers of double-layers n, each consisting of 16 nm Ag and 250 nm SiO_2.

depicted in Fig. 3.3(b). It can be clearly seen that the nodes of the electric field inside the structure are located in or close to the metal layers. Also a large field intensity enhancement inside the structure by a factor of 16 (4 for the electric field strength) is evident. For comparison, the field intensity as a function of the penetration depth in one silver layer of equivalent thickness is plotted in Fig. 3.3(a). The wavelength (about 800 nm) chosen for these calculations corresponds to the maximum transmission peak of the 1DMDPC structure (cf. Fig. 3.2).

Simulated linear transmission spectra for different numbers of layer pairs are shown in Fig. 3.4. They show that in the ideal case the maximum transmission does not considerably change with the number of layers. These and other simulations also show that the spacer layer thickness mainly governs the peak positions while the number of layers determines the number of peaks and their widths. The spacer layer thickness times its refractive index is typically slightly smaller than half the wavelength corresponding to the main transmission peak. Thus, the position of the maximum transmission wavelength can be described as a Bragg condition quite well. For the other peaks, however, such a simple picture does not suffice to explain their spectral position. However, the structure can simply be modeled as coupled oscillators or coupled optical cavities whose normal modes correspond to the additional transmission peaks and can particularly explain the number of peaks for a given number of layers. For the experiments, the number of double-layers was set to five as recommended in Ref. [11]. In the following, all 1DMDPCs mentioned have five metal and five dielectric layers unless explicitly stated otherwise.

3.3. Samples and experimental setup

3.3.1. Sample fabrication

The 16-nm-thick silver layers have been grown using electron beam physical vapor deposition (EBPVD) with a thickness deviation of about ±2 nm. The spacer layers out of silicon dioxide have been fabricated using plasma-enhanced chemical vapor deposition (PECVD). This has proved to be a good choice leading to high quality layers with very low thickness fluctuations smaller than 2% as measured by a commercial white light interferometry system on a piece of silicon wafer placed beside the sample in each evaporation process. As the substrate for the structure fused silica (Herasil) has been chosen.

The growth techniques used to manufacture the 1DMDPCs are neither new nor the topic of this work. Therefore the following description of them is kept very short:

EBPVD uses a focused electron beam to evaporate the coating material. The film growth is obtained by condensation of the vapor on a substrate mounted upside down above the material tray. The deposition chamber is evacuated before starting the evaporation process. The growth rate is controlled by adjusting the current of the electron beam, thus regulating the thermal energy intake.

For the fabrication of the silicon dioxide layers, electron cyclotron resonance (ECR) PECVD was used. This method is a low-temperature growth technique for dielectric films, typically SiO_2 and SiN_x. It involves using microwave radiation together with a static magnetic field to generate a plasma by exciting the electron cyclotron resonance of the process gas electrons. The gases used to deposit SiO_2 layers are silane (SiH_4) diluted in argon and nitrous oxide (N_2O). PECVD is well known for its stable and high deposition rate. The film thickness is controlled by the irradiation time of the microwave source.

Using the techniques described above, it was possible to achieve a transmission maximum of 45% for a five metal layer structure as shown in Fig. 3.5. The overall shape of the measured transmission spectrum is remarkably close to the simulated one [Fig. 3.2]. This verifies the good quality of the samples.

However, the good quality could not be easily maintained over a long period of time. Silver normally does not react with oxygen but tends to undergo

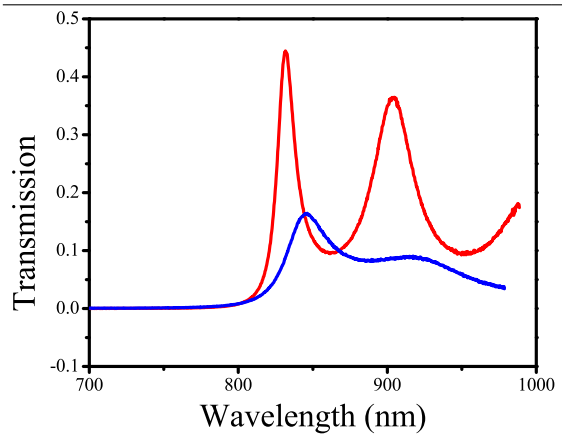

Figure 3.5.: Measured transmission spectra of a silver-based 1DMDPC directly after fabrication (red curve) and after eight month (blue curve).

a chemical reaction with other components residing in air, especially H_2S. The thin top layer of only 250 nm silicon dioxide proved to be unable to protect the silver layers underneath for a long time. Figure 3.5 shows the transmission spectra of a silver-based 1DMDPC shortly after fabrication and after eight months. Although the sample was kept in vacuum most of the time when it was not used, a considerable decrease in the transmission can be observed. The red shift of the transmission peak suggests that mostly the fifth silver layer has degraded. This means that such a sample will behave more like a four layer 1DMDPC with increasing age.

3.3.2. Pump-probe setup

The setup used for the time-resolved transmission measurements is depicted in Fig. 3.6. It is based on the well-known pump-probe spectroscopy principle. In all experiments, a Titanium:Sapphire oscillator (Coherent Mira 900) served as light source. It delivers 100 fs full width at half maximum (FWHM) pulses at a repetition rate of 76 MHz. The laser wavelength can be tuned in a range from 790 nm to 900 nm. The output beam is split into two parts of which one is delayed with respect to the other in a variable delay line. Both beams are focused onto the same spot on the surface of the sample. The spot size (FWHM) is typically around 16 μm. Since the optical path length between the metal layers governs the wavelength with maximum transmission, a strong dependence of the peak position on the angle between the sample surface normal and the incident beam is expected. Measurements of the angular dependence of the transmission peak

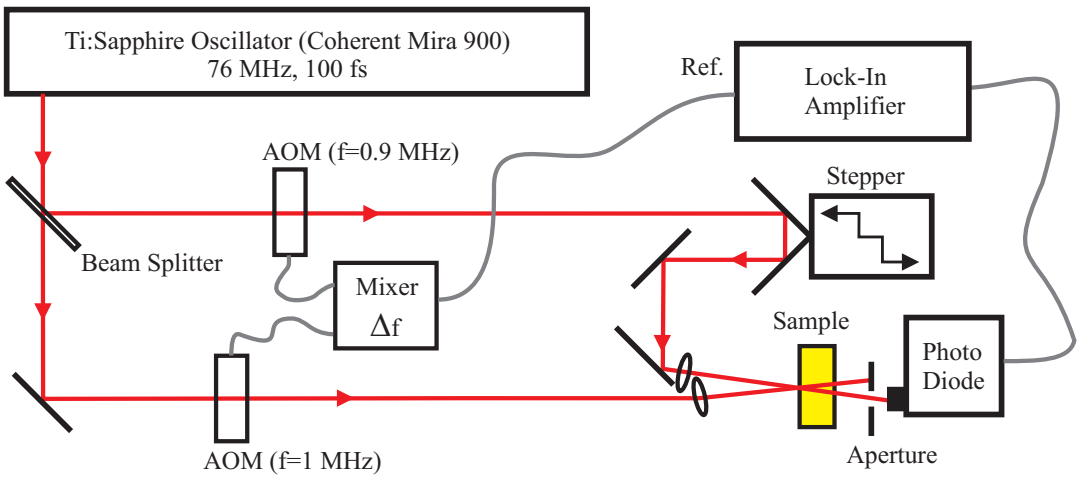

Figure 3.6.: The double-modulation pump-probe setup.

[Fig. 3.7] confirm this. In experimental setup, the angle is adjusted to be as small as possible, more precisely to about 5°. For such a small angle the shift of the transmission spectrum is negligible. Incidence at 0° for both beams is not possible due to the fact that the pump and probe beam must be spatially separated to measure only the probe intensity. The probe beam is detected by a photo diode. The pump beam, whose intensity is about three orders of magnitude higher, is blocked by an aperture between the sample and the diode. All experiments presented in this chapter are performed at room temperature.

To achieve the necessary signal to noise ratio, pump and probe beams are intensity-modulated using acousto-optic modulators (AOMs) for detection with a lock-in amplifier. The modulation frequencies are 900 kHz and 1000 kHz, respectively. The reason for modulating both beams is that this way the measured signal is proportional to the differential transmission ΔT instead of to the absolute transmission T (which is several orders of magnitude higher). The high modulation frequencies ensure that the $\frac{1}{f}$-noise is small. Additionally, the sample temperature change between the pump-on and the pump-off state is minimized. The output of the photo diode is amplified by a low-noise current amplifier (FEMTO DLPCA-200) and measured by a lock-in amplifier (Stanford Research Systems SR830) which uses the difference frequency as its reference. This way it measures the change of the probe signal induced by the pump beam (and vice versa but the pump beam intensity is three orders of magnitude higher) and avoids the influence of noise generated by each beam. The lock-in phase was calibrated by replacing

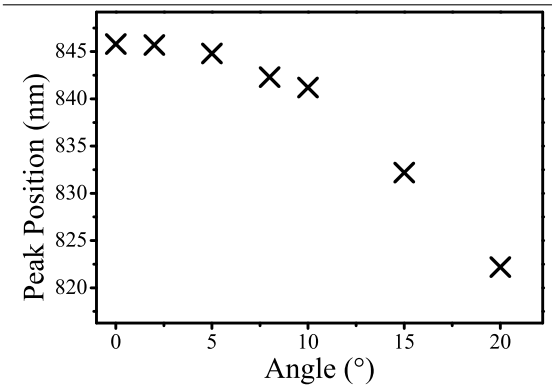

Figure 3.7.: Angular dependence of the transmission maximum position measured on a silver-based 1DMDPC.

the sample by a nonlinear crystal (β-Barium-Borate) and tuning the phase to the maximum upconverted power. The lock-in output signal was recorded by a computer as a function of the stepper position in the delay line. It is important to keep in mind that the signal recorded by the lock-in amplifier is reduced by a factor of two with respect to the real signal due to the fact that the signal component at the sum frequency of the two modulation signals is neglected.

The intensities given in this chapter are calculated as follows:
For each measurement the average pump beam power $\bar{P}$ is recorded, i.e., about half the peak power of the sine wave-modulated beam. Together with the repetition rate f_{rep}, the temporal FWHM τ, and the spatial FWHM w_0 at the focus, the pump intensity I as power per unit area is estimated by:

$$I = \frac{\bar{P}}{f_{rep} \cdot \tau \cdot \pi \cdot (w_0/2)^2}. \tag{3.3}$$

This yields an intensity of 660 MW/cm^2 per 10mW average power.

3.4. Time-resolved measurements

3.4.1. Real time measurements

To determine the magnitude of the nonlinear transmission changes in the 1DMDPCs, the unmodulated probe signal was first directly detected in real time while the pump beam was switched on and off periodically at a frequency of 0.1 Hz. From previous experiments (e.g. Ref. [11]) the nonlinear transmission suppression was expected to be on the order of up to several tenths of the maximum transmission. The differential transmission as a function of time for a silver-based 1DMDPC is shown in Fig. 3.8(a). The maximum reduction at 1600 MW/cm^2 is around 14%. A fit of the recovery characteristics [Fig. 3.8(b)] with an exponential decay function ($c_0 + c_1 \cdot \exp(-t/t_1)$) yields a time constant t_1 of 740 ms. This slow recovery behavior is a clear evidence that the reason for the strong transmission decrease is not a microscopic effect, but rather macroscopic heating of the sample. The fact that such a strong transmission change was neither observed in a dielectric material nor in a single metal layer can be explained as follows: A thermal expansion of the layers in the structure leads to a violation of the periodicity condition needed for a transmission band at the incident light wavelength. Therefore, due to the detuning of the Bragg condition, the transmission is considerably decreased.

The results presented here raise the question whether the z-scan measurements in Ref. [11] have also been just a result of sample heating, and how strong the proposed Fermi smearing effect is compared to the macroscopic heating. Concluding from the measurements presented here, the ultrafast effect due to the carrier redistribution must be considerably smaller than the observed heating effects. For this reason the double-modulation pump-probe scheme described in section 3.3.2 needs to be employed as it can efficiently separate fast from slow effects. Scaling the 14% effect with the 740 ms decay time down to one period of the pump modulation yields $\Delta T/T = 2 \times 10^{-6}$. The pump-probe results are presented in the following section.

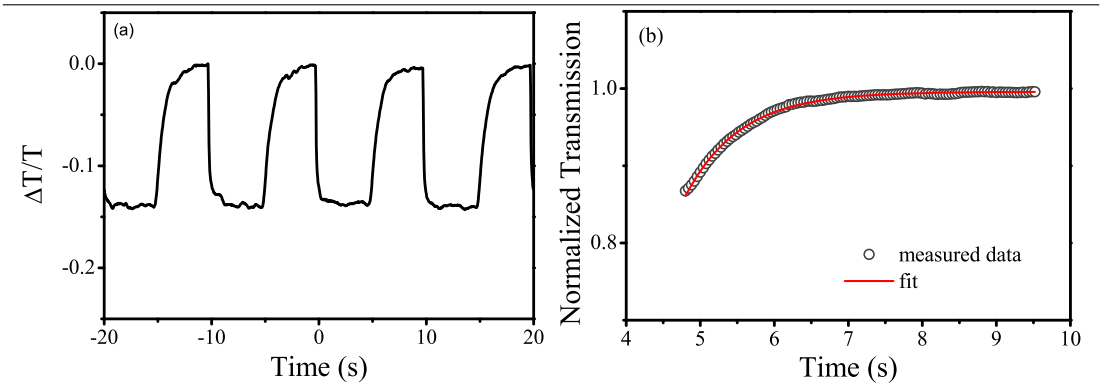

Figure 3.8.: (a) Real-time measurement of the differential transmission when the pump beam is modulated by a square wave at 0.1 Hz. (b) Recovery characteristics of the sample transmission fitted by an exponential decay function (time constant 740 ms).

3.4.2. Pump probe results

The main goal of the experiments presented in this section was to find fast effects that should exist on top of the slow thermal effects described above. The differential transmission as a function of the delay between pump and probe beam have been measured by means of the double-modulation pump-probe technique (cf. section 3.3.2). The results for different pump intensities are depicted in Fig. 3.9. The central laser wavelength was tuned slightly lower than the transmission peak position, because the fast nonlinear response was perceived to be the strongest there. An objective measure of the maximum effect with respect to the excitation wavelength cannot be given due to the fact that the wavelength dependence is small compared to the noise level. The spectral width of the laser was about 8 nm and the width of the transmission window around 15 nm.

The most interesting feature in Fig. 3.9 is certainly the fast negative transmission change starting around zero delay. The transmission drops to a minimum within a few hundred femtoseconds. Subsequently, it recovers by following an exponential decay function for about half a picosecond. This is slightly faster than the decay time reported for single copper and silver films [52]. The value of the decay time of about one picosecond is an indication that the mechanism behind this effect is fast heating (on the order several hundreds of Kelvins) of the electron gas in the metal layers as described in section 3.2. It typically takes this

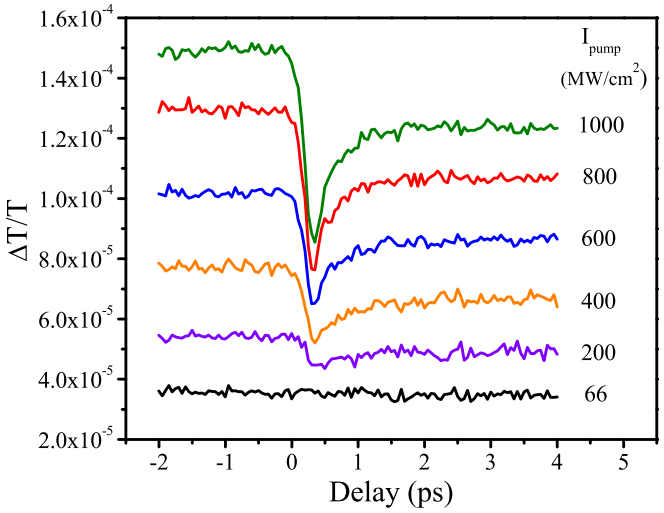

Figure 3.9.: Differential transmission $\Delta T/T$ measured by pump-probe spectroscopy as a function of the delay between the pump and the probe pulse. The background signal is pump intensity dependent and can also be observed if the probe beam is blocked. The employed pump intensities (in MW/cm^2) are: 66 (black), 200 (purple), 400 (orange), 600 (blue), 800 (red), 1000 (green).

amount of time for the electron gas to thermalize with the lattice. Nonlinear effects in the silicon dioxide layers such as the Kerr effect most probably play no significant role here since their recovery would be instantaneous, i.e., the evolution of transmission would follow the field envelope of the pump pulse and not decay exponentially. The fact that the multi-layer structure is only one μm long (corresponding to a light propagation time of about 5 fs assuming a refractive index of 1.5) indicates that it is also very unlikely that the pump pulse remains inside the structure for several hundred femtoseconds. Since the heat capacity of the lattice is much higher, the lattice temperature after thermalization is only a few Kelvins higher than before. However, even this relatively small temperature increase prevents the full recovery of the fast effect: The background signal in Fig. 3.9 exhibits a difference between the values at the highest and the lowest delays. The background signal is a superposition of three mechanisms. First of all, there is already a nonzero signal caused by the probe beam when them pump beam is completely shut off. Secondly, the scattered pump light causes a signal increase depending on its intensity. This is also the case if the probe beam is

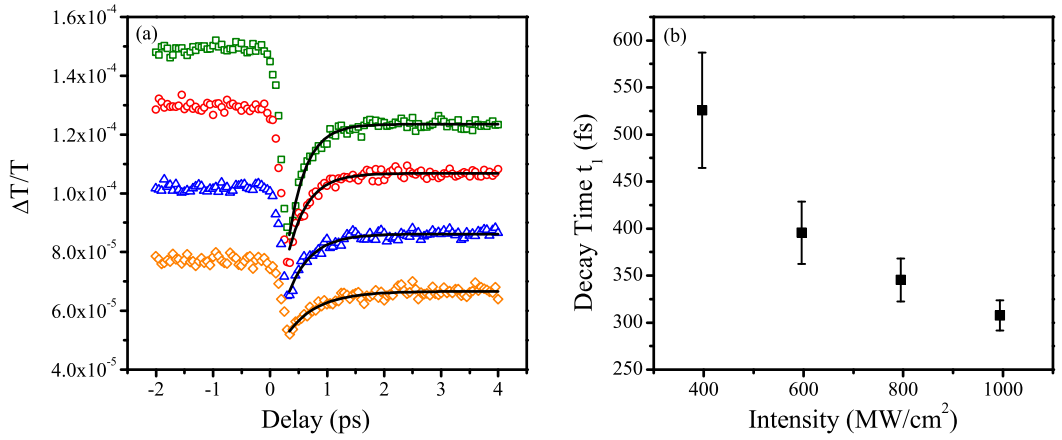

Figure 3.10.: (a) The four upper curves of Fig. 3.9 fitted with an exponential decay function. (b) Decay time t_1 as a function of the pump intensity.

shut off. If the sample is removed, this contribution vanishes. In principle, there should be no signal at the difference frequency of the two modulations if only one beam is present. The most self-evident explanation would be high frequency fluctuations of scattered pump light. However, these artifacts are delay independent and thus not relevant for the interpretation of the temporal dynamics. The third effect, i.e., the signal difference between the highest and the lowest delays, is dependent on the pump intensity and the delay. Due to the fact that the temporal distance between two pump pulses is 13 ns, the signal several picoseconds before and after the overlap is different because cooling of the lattice can take place between two pulses. Heating the lattice causes a negative transmission change as expected from the real time measurements.

An exponential decay fit of the ultrafast nonlinear transmission characteristics clearly shows a dependence of the relative transmission reduction on the pump power. Between the lowest and the highest measured intensity the decay time is reduced by almost a factor of two. One has to be very careful with such signal fitting since the behavior of the nanosecond lattice effect superimposed with the femtosecond electron gas heating induced effect is not exactly known. To verify that the results for the intensity dependence of the decay time t_1 shown in Fig. 3.10(b) are qualitative correct, additionally an alternative fitting method was employed: To exclude the lattice effect from the fit it was approximated by an exponential decay function (the black curves in Fig. 3.11(a)) fitted to each of

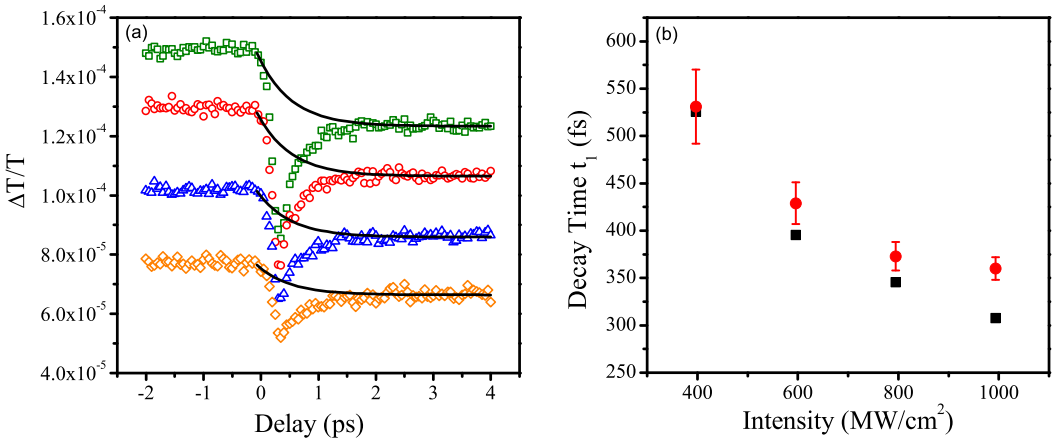

Figure 3.11.: (a) The exponential decay functions (black curves) subtracted for the alternative fits (see text). (b) Results of the alternative fits (red circles) compared to the initial fits (black squares) as shown in Fig. 3.10.

the curves using the same decay time ($t_2 = 570$ fs[1]) for all curves. These functions where then subtracted from the data before another set of fits was made. This is equivalent to fitting the data with the sum of two exponential decay functions $(c_0 + c_1 \cdot \exp(-t/t_1) + c_2(1 - \exp(-t/t_2)$. The results are plotted in Fig. 3.11(b) (black squares) together with the those from the previous fits (red circles) for comparison. All decay time values are higher than the previous ones but the qualitative result, namely the decrease of the decay time with increasing intensity, is still clearly visible.

[1]The choice of this value is based on a rough guess and by no means intended to be used to describe the lattice dynamics. It is only meant as a best effort to separate electron gas and lattice effects.

3.5. Discussion and outlook

The experiments presented in this chapter essentially produced two very interesting results:

First, they did not show one strong, fast effect but essentially two effects on completely different time and magnitude scales which govern the nonlinear transmission changes in 1DMDPCs. A transmission decrease on the order of 15% with a recovery time of several hundred milliseconds as well as a small ultrafast transmission reduction on the order of $5 \cdot 10^{-5}$ with a recovery time of around 500 fs have been observed. The latter can be attributed to the Fermi smearing [11] nonlinearity: For the duration of the incident 100 fs pulse, the electron gas in the metal layers is strongly heated while the lattice practically keeps its temperature. It then takes about one picosecond for electron gas and lattice to reach thermal equilibrium, mainly by electron-phonon scattering [52]. Due to the repetition rate of the laser source, the lattice has about 13 ns to cool down before the next pulse hits the sample. As the real time measurements have shown, it takes considerably longer to bring the sample back to the initial state, more precisely this will take almost one second. Thus, due to the energy intake of the subsequent pulses, the whole sample is heated which leads to an expansion of the metal and the dielectric layers and thereby to a detuning of the Bragg condition. The condition for the transmission window is thereby violated, leading to a considerable decrease in transmission. The change induced by this effect exceeds the influence of the fast electron gas heating on the transmissive properties of the multi-layer structure by more than three orders of magnitude. It is very likely that the strong transmission suppression observed in pervious z-scan measurements [11] is also due to thermal expansion. This high sensitivity to macroscopic heating is clearly a weakness of the concept with respect to applications.

Secondly, for the ultrafast effect the dependency of the decay time (the time it takes for the electron gas to thermalize with the lattice) on the pump power was observed to be opposite to previous experiments on *single* metal layers [58]. In the experiments shown here, the fastest decay was observed for the highest pump intensities. Those presented in Ref. [58] (albeit at higher pump intensities) show an increase in the decay time for increasing pump intensity. This is also what one would expect applying the two-temperature model [55]. The reason

for the behavior in the multi-layer structures is still unclear. Future experiments which investigate the dependence of this effect on the number of layer pairs could bring important insight into this open question.

These two results are clearly an achievement of the time-resolved experiments and could not be deduced from z-scan measurements alone. They also indicate that theoretical models which neglect heat transport and memory effects are insufficient to calculate the real properties of 1DMDPCs. Modified models could be very helpful to ultimately resolve the question whether it is possible to increase the strength of the ultrafast effect to a degree sufficient for ultrafast applications. Higher pump power may shift the balance between the slow and the fast but will most surely decrease the lifetime of the sample. Z-scan measurements using a microscope objective (not shown) revealed that the powers used here are already quite close (within one order of magnitude) to the destruction threshold of the structures. Lowering the laser repetition rate would lead to less or slower sample heating. But considering the goal to develop a concept for optical switching on a picosecond scale, it does not make much sense to have a picosecond switch that can only be used every 100 ns or even less. Possible solutions to increase the electron gas heating induced effect with respect to the slow bulk effect could lie in the choice of other materials and/or a different number of layers. Also, choosing a different pump wavelength closer to interband transitions might have a positive influence. The transmission window of the samples can easily be shifted by adjusting the dielectric spacer layer thickness. Its width can be set by the number of layer pairs. Recent experiments on gold films [59] show a strong dependence of the nonlinear response on the incident pulse length. Therefore, the pump pulse length should also be taken into account in future efforts to improve the applicability of 1DMDPCs.

Chapter 4
Summary

In this thesis, investigations of two classes of one-dimensional (1D) photonic crystals (PCs) have been presented:

(1) Semiconductor multiple-quantum-well (MQW) Bragg structures, which are resonant PCs (Chapter 2): The investigated samples are high-quality MQW structures which contain 60 $In_{0.04}Ga_{0.96}As$ quantum wells (QWs) grown on a GaAs substrate. The QWs are periodically spaced with GaAs barrier layers whose thicknesses are adjusted to satisfy the Bragg condition for the lowest heavy-hole exciton resonance at $\lambda_{ex} = 830$ nm for propagation perpendicular to the QWs. For comparison, also bulk GaAs crystals without any artificial structuring have been studied in detail. The results have provided a deeper understanding of light-matter interaction in semiconductor structures as well as to differentiate QW-induced effects from those caused by the bulk part of the MQW structure. A pulse propagation measurement technique at low temperature (10 K) has been applied, which is based on a sophisticated fast-scanning cross-correlation frequency-resolved optical gating (XFROG) [10] scheme. It delivers the time-dependent amplitude and phase of the propagated laser pulses with an outstanding signal-to-noise ratio.

(2) Metal-dielectric PCs (Chapter 3): The metal-dielectric PC system discussed in chapter 3 consists of 5 periodically arranged 16 nm-thick silver layers separated by 250-nm-thick silicon dioxide spacer layers. The transmission dynamics of this system has been investigated using sub-picosecond pump-probe spectroscopy at room temperature.

The focus of all studies has been on characterizing the sub-picosecond temporal dynamics of fundamental light-matter interaction processes and reviewing their potential with respect to applications such as all-optical switching and pulse shaping.

At the time the presented research began, semiconductor (SC) MQW Bragg structures had already been proven to be of great scientific interest for ultrafast optics in the spectral region around their photonic band gap (PBG). The PBG in these structures is due to the formation of a superradiant mode by radiative coupling of the QWs. Previous works had shown that they feature an ultrafast recovery effect which is of great interest for the design of an all-optical switching device with possibly a terahertz switching rate [5, 6]. Also, with respect to pulse shaping, i.e., controlled manipulation of the pulse profile, ultrafast propagation experiments [9] had surprisingly revealed that gap solitons cannot be expected in SC MQW Bragg structures as predicted for resonant PCs in general [7, 8]. The reason had been found to be the break-down of the PBG at moderately high input pulse intensities. In this thesis, the knowledge about these structures has been greatly expanded and several then open questions have been answered: What effects occur at higher intensities beyond the PBG break-down? This has been answered in section 2.3 by presenting phase-resolved pulse propagation measurements: self-induced transmission and strong self-phase modulation (SPM) exhibiting soliton-like pulse components have been observed. Which role do the QWs play in the intensity regimes where the PBG is strongly suppressed? In section 2.4, a clear distinction between QW-induced effects and those predominantly caused by the bulk part of SC MQW Bragg structures[1] could be made by a detailed study of ultrashort pulse propagation in bulk SCs. The precise differentiation and characterization of the involved phenomena have benefited considerably from the attainment of the previously completely unknown pulse phase dynamics. The knowledge of the complete modification of pulse phase and envelope after propagation has delivered a deep insight into the transitions between the intensity regimes, from linear propagation (characterized by a pronounced temporal beating due to the interference of spectral components transmitted on both sides of the PBG) to the breakdown of the PBG due to Pauli-blocking, to self-induced transmission (by Rabi flopping of the carrier density), and–at the highest

[1] bulk part here refers to the substrate and the spacer layers, in which the spacer layer thickness is rather negligible

applied intensities–to a SPM-induced beating. These fundamental light-matter interaction effects are usually observed in very different material systems. Thus, this work is exemplary for the interplay of the interaction phenomena and is, therefore, also relevant for many other PC- and SC-structures. The SPM that occurs at high input intensities could be clearly attributed to the bulk part of the sample. An influence of the QWs in this regime could merely be seen in partial suppression of the phase jumps between the individual pulse components. This finding is an achievement of the comprehensive analysis of near-resonant SPM on pulse propagation in bulk GaAs at low temperature presented in the second part of chapter 2. There, a detailed overview of the interplay of SPM in the negative n_2 regime with normal dispersion in SCs has been given. This has been investigated in dependence on the propagation length, the input pulse intensity, the focusing into the sample, and the detuning from the band edge. The observations include a pronounced pulse compression by more than a factor of two and the formation of a pulse train by strong SPM, which features soliton-like behavior of the main pulse, i.e., balancing of the normal material dispersion and the defocusing nonlinearity. A possible application for the observed pulse compression effect are semiconductor laser diodes which could use the knowledge gained about SPM in SCs to realize intrinsic pulse compression as suggested in Ref. [28].

The experimental findings concerning the MQW structures were supported by a comparison with calculations solving the semiconductor Maxwell-Bloch equations (SMBE) in collaboration with M. Schaarschmidt, J. Förstner and A. Knorr from the Technische Universität Berlin and S. W. Koch from the Philipps-Universität Marburg. The experimental observations on bulk GaAs have been compared to numerical simulations based on a home-made Matlab program which numerically solves the nonlinear Schrödinger equation (NLSE). In spite of the simplicity of this model, the results have shown a surprisingly well qualitative agreement with the experimental results.

Many of the results shown in chapter 2 have been published in Refs. [30] and [31].

The second material system investigated, as discussed in chapter 3, is a one-dimensional metal-dielectric photonic crystal (1DMDPC). These structures have considerable advantages over the SC MQW structures. While the SC structures require low temperatures (on the order of 10 K) to show the desired effects, 1DMDPCs can be used at room temperature. Additionally, the number of layers

needed is considerably smaller. The SC MQW Bragg structures typically contain 60-200 QWs [5, 9], 1DMDPCs usually need only 5 metal layers [11]. Recent publications [11–17] contain clear indications of a high potential of 1DMDPCs for ultrafast all-optical switching applications. The unique feature of 1DMDPCs that allows for exploiting the nonlinear transmissive properties of metals is a transparency band which they exhibit even if the accumulated thickness of the metal layers is increased to multiples of the skin depth in bulk metal [13, 48, 49]. Recent experiments [11], using the well-known open-aperture z-scan technique [50], had reported a nonlinear suppression of the transmission by a factor of 2.5 and suggest a recovery time on the order of one picosecond (as observed in pump-probe measurements on single metal films [52]). Numerical calculations [15] had predicted switching of the transmission between 60% and 5% in 1DMDPCs.

The results presented in chapter 3 constitute the first experimental time-resolved studies on the transmission dynamics in 1DMDPCs. As the main measurement technique, pump-probe spectroscopy with sub-picosecond time resolution has been employed. The results have provided new insights into the fundamental dynamics and revealed strengths and weaknesses of the concept with respect to ultrafast all-optical switching applications. The experiments have shown essentially two effects on completely different time and magnitude scales which govern the nonlinear differential transmission. A transmission decrease on the order of 15% with a recovery time of several hundred milliseconds as well as a small relative transmission reduction on the order of $5 \cdot 10^{-5}$ with a recovery time of about 500 fs have been observed. The slow effect can be attributed to heating of the whole structure which causes a thermal expansion and thereby a modification of the condition for the transmission window leading to a considerable decrease in transmission. It is very likely that the strong transmission suppression observed in previous z-scan measurements [11] is also due to thermal expansion. This high sensitivity to macroscopic heating is likely a weakness of the concept with respect to applications. The fast effect on the other hand can be attributed to the Fermi smearing [11] nonlinearity: For the duration of the incident 100 fs pulse, the electron gas in the metal layers is strongly heated while the lattice keeps its temperature. It then takes about one picosecond for electron gas and lattice to reach a common thermal equilibrium [52]. Thus, the observations presented in this thesis confirm that a nonlinear transmission suppression with fast response and recovery is possible in such a structure. However, the differential transmis-

sion was found to be only on the order of $5 \cdot 10^{-5}$. Surprisingly, the fast effect has shown an unexpected dependence of the decay time (the time it takes for the electron gas to thermalize with the lattice) on the pump power which is contrary to previous experiments on single metal layers [58]. The fastest decay has been observed for the highest pump intensities. The reason for this behavior in the multi-layer structures remains an open question. Future experiments which investigate the dependence of this effect on the number of layer pairs could bring new insight. The knowledge gained from the observations in chapter 3 is clearly an achievement of the time-resolved experiments and could not be deduced from z-scan measurements. The results indicate that models commonly used to describe the dynamics in metal nano-particles and thin films (such as the two temperature model [55]) are insufficient to describe ultrafast effects in 1DMDPCs. The results of this thesis are certainly a good guidance to find modified models that are able to explain the ultrafast transmission dynamics. They may also be of considerable help with respect to improving the applicability of 1DMDPCs for ultrafast all-optical switching devices.

References

[1] H. Grabert and H. Horner (eds.), *Special Issue on Single Charge Tunnelling*, Z. Phys. B **85**, 317 (1991).

[2] L. Brillouin, *Wave Propagation in Periodic Structures* (McGraw-Hill, 1946).

[3] H. G. Winful, *Pulse compression in optical fiber filters*, Appl. Phys. Lett. **46**, 527 (1985).

[4] B. J. Eggleton, R. E. Slusher, C. Martijn de Sterke, P. A. Krug, and J. E. Sipe, *Bragg Grating Solitons*, Phys. Rev. Lett. **76**, 1627 (1996).

[5] J. P. Prineas, J. Y. Zhou, J. Kuhl, H. M. Gibbs, G. Khitrova, S. W. Koch, and A. Knorr, *Ultrafast ac Stark effect switching of the active photonic band gap from Bragg-periodic semiconductor quantum wells*, Appl. Phys. Lett. **81**, 4332 (2002).

[6] M. Schaarschmidt, J. Förstner, A. Knorr, J. P. Prineas, N. C. Nielsen, J. Kuhl, G.Khitrova, H. M. Gibbs, H. Giessen, and S. W. Koch, *Adiabatically driven electron dynamics in a resonant photonic band gap: optical switching of a Bragg periodic semiconductor*, Phys. Rev. B **70**, 233302 (2004).

[7] W. Chen and D. L. Mills, *Gap solitons and the nonlinear optical response of superlattices*, Phys. Rev. Lett. **58**, 160 (1987).

[8] A. B. Aceves and S. Wabnitz, *Self-induced transparency solitons in nonlinear refractive periodic media*, Phys. Lett. A **141**, 37 (1989).

[9] N. C. Nielsen, J. Kuhl, M. Schaarschmidt, J. Förstner, A. Knorr, S. W. Koch, G. Khitrova, H. M. Gibbs, and H. Giessen, *Linear and nonlinear pulse propagation in a multiple-quantum-well*, Phys. Rev. B **70**, 075306 (2004).

[10] S. Linden, H. Giessen, and J. Kuhl, *XFROG - A New Method for Amplitude and Phase Characterization of Weak Ultrashort Pulses*, Phys. Stat. Sol. (b) **206**, 119 (1998).

[11] Nick N. Lepeshkin, Aaron Schweinsberg, Giovanni Piredda, Ryan S. Bennink, and Robert W. Boyd, *Enhanced Nonlinear Optical Response of One-Dimensional Metal-Dielectric Photonic Crystals*, Phys. Rev. Lett. **93**, 123902 (2004).

[12] Xiaochuang Xu, Yonggang Xi, Dezhuan Han, Xiaohan Liu, Jian Zia, and Ziqiang Zhu, *Effective plasma frequency in one-dimensional metallic-dielectric photonic crystals*, Appl. Phys. Lett. **86**, 091112 (2005).

[13] Ryan S. Bennink, Young-Kwon Yoon, and Robert W. Boyd, *Accessing the optical nonlinearity of metals with metal-dielectric photonic bandgap structures*, Opt. Lett. **24**, 1416 (1999).

[14] A. Benabbas, V. Halté, and J.-Y. Bigot, *Analytical model of the optical response of periodically structured metallic films*, Opt. Express **13**, 8730 (2005).

[15] Michael Scalora, Nadia Mattiucci, Giuseppe D'Aguanno, Maria Cristina Larciprete, and Mark J. Bloemer, *Nonlinear pulse propagation in one-dimensional metal-dielectric multilayer stacks: Ultrawide bandwidth optical limiting*, Phys. Rev. E **73**, 016603 (2006).

[16] M. C. Larciprete, C. Sibilia, S. Paoloni, M. Bertolotti, F. Sarto, and M. Scalora, *Accessing the optical limiting properties of metallo-dielectric photonic band gap structures*, J. Appl. Phys. **93**, 5013 (2003).

[17] Tammy K. Lee, Alan D. Bristow, Jens Hübner, and Henry M. van Driel, *Linear and nonlinear optical properties of Au-polymer metallodielectric Bragg stacks*, J. Opt. Soc. Am. B **23**, 2142 (2006).

[18] H. Ju, S. Zhang, H. de Waardt, E. Tangdiongga, G. D. Khoe, and H. J. S. Dorren, *SOA-based all-optical switch with subpicosecond full recovery*, Optics Express **13**, 942 (2005).

[19] J. P. Reithmaier, G. Sek, A. Löffler, C. Hofmann, S. Kuhn, S. Reitzenstein, L. V. Keldysh, V. D. Kulakovskii, T. L. Reinecke, and A. Forchel, *Strong*

coupling in a single quantum dot-semiconductor microcavity system, Nature **432**, 197 (2004).

[20] G. Ortner, I. Yugova, A. Larionov, H. V. G. Baldassarri, M. Bayer, P. Hawrylak, S. Fafard, and Z. Wasilewski, *Coherent optical control of semiconductor quantum dots for quantum information processing*, Physica E **25**, 242 (2004).

[21] Y. W. Wu, X. Q. Li, D. Steel, D. Gammon, and L. J. Sham, *Experimental demonstration of coherent coupling of two quantum dots*, Physica E **26**, 281 (2005).

[22] R. Trebino, *Frequency-Resolved Optical Gating: The Measurement of Ultrashort Laser Pulses* (Kluwer Academic Publishers, 2002).

[23] J. S. Nägerl, B. Stabenau, G. Böhne, S. Dreher, R. G. Ulbrich, G. Manzke, and K. Henneberger, *Polariton pulse propagation through GaAs: Excitation-dependent phase shifts*, Phys. Rev. B **63**, 235202 (2001).

[24] N.C. Nielsen, T. Höner zu Siederdissen, J. Kuhl, M. Schaarschmidt, J. Foerstner, A. Knorr, and H. Giessen, *Phase evolution of solitonlike optical pulses during excitonic Rabi flopping in a semiconductor*, Phys. Rev. Lett. **94**, 057406 (2005).

[25] F. G. Omenetto, B. P. Luce, D. Yarotski, and A. J. Taylor, *Observation of Chirped Soliton Dynamics at Lambda=1.55 μm in a Single-Mode Optical Fiber with Frequency-Resolved Optical Gating*, Opt. Lett. **24**, 1392 (1999).

[26] H. Giessen, A. Knorr, S. Haas, S. W. Koch, S. Linden, J. Kuhl, M. Hetterich, M. Grün, and C. Klingshirn, *Self-Induced Transmission on a Free Exciton Resonance in a Semiconductor*, Phys. Rev. Lett. **81**, 4260 (1998).

[27] P. A. Harten, A. Knorr, J. P. Sokoloff, F. Brown de Colstoun, S. G. Lee, R. Jin, E. M. Wright, G. Khitrova, H. M. Gibbs, S. W. Koch, and N. Peyghambarian, *Propagation-Induced Escape from Adibatic Following in a Semiconductor*, Phys. Rev. Lett. **69**, 852 (1992).

[28] J.-F. Lami, S. Petit, and C. Hirlimann, *Self-Steepening and Self-Compression of Ultrashort Optical Pulses in a Defocusing CdS Crystal*, Phys. Rev. Lett. **82**, 1032 (1999).

[29] P. Dumais, A. Villeneuve, and J. S. Aitchison, *Bright temporal solitonlike pulses in self-defocusing AlGaAs waveguides near 800 nm*, Opt. Lett. **21**, 260 (1996).

[30] T. Höner zu Siederdissen, N.C. Nielsen, J. Kuhl, M. Schaarschmidt, J. Foerstner, A. Knorr, G. Khitrova, H.M. Gibbs, S.W. Koch, and H. Giessen, *Transition between different coherent light-matter interaction regimes analyzed by phase-resolved pulse propagation*, Opt. Lett. **30**, 1384 (2005).

[31] T. Höner zu Siederdissen, N. C. Nielsen, J. Kuhl, and H. Giessen, *Influence of near-resonant self-phase modulation on pulse propagation in semiconductors*, J. Opt. Soc. Am. B **23**, 1360 (2006).

[32] G. P. Agrawal, *Nonlinear Fiber Optics* (Academic Press, 1995).

[33] J.-C. Diels and W. Rudoph, *Ultrashort Laser Pulse Phenomena* (Academic Press, 1996).

[34] S. Das Sarma, R. Jalabert, and S.-R. E. Yang, *Band-gap renormalization in semiconductor quantum-wells*, Phys. Rev. B **41**, 8288 (1990).

[35] N. C. Nielsen, S. Linden, J. Kuhl, J. Förstner, A. Knorr, S. W. Koch, and H. Giessen, *Coherent nonlinear pulse propagation on a free-exciton resonance in a semiconductor*, Phys. Rev. B **64**, 245202 (2001).

[36] K. Tai, S. Hasegawa, and A. Tomita, *Observation of modulational instability in optical fibers*, Phys. Rev. Lett. **56**, 135 (1986).

[37] M. Lindberg and S. W. Koch, *Effective Bloch Equations for Semiconductors*, Phys. Rev. B **38**, 3342 (1988).

[38] K. Yee, *Numerical solution of initial boundary value problems involving maxwells equations in isotropic media*, IEEE Transactions on Antennas and Propagation **14**, 302 (1966).

[39] L. Allen and J. H. Eberly, *Optical Resonance and Two-Level Atoms* (John Wiley & Sons, 1975).

[40] A. Knorr, R. Binder, M. Lindberg, and S. W. Koch, *Theoretical Study of Resonant Ultrashort-Pulse Propagation in Semiconductors*, Phys. Rev. A **46**, 7179 (1992).

[41] M. Sheik-Bahae, D. C. Hutchings, D. J. Hagan, and E. W. van Stryland, *Dispersion of Bound Electronic Nonlinear Refraction in Solids*, IEEE J. Quantum Electron. **27**, 1296 (1991).

[42] R. L. Sutherland, *Handbook of Nonlinear Optics* (Marcel Dekker, Inc., 1996).

[43] A. E. Kozhekin, G. Kurizki, and B. Malomed, *Standing and Moving Gap Solitons in Resonantly Absorbing Gratings*, Phys. Rev. Lett. **81**, 3647 (1998).

[44] T. Opatrny, B. A. Malomed, and G. Kurizki, *Dark and bright solitons in resonantly absorbing gratings*, Phys. Rev. E **60**, 6137 (1999).

[45] W. N. Xiao, J. Y. Zhou, and J. P. Prineas, *Storage of ultrashort optical pulses in a resonantly absorbing Bragg reflector*, Optics Express **11**, 3277 (2003).

[46] J. Y. Zhou, Q. Lan, J. Zhang, J. T. Li, J. H. Zeng, J. Cheng, I. Friedler, and G. Kurizki, *Nonlinear dynamics of negatively refracted light in a resonantly absorbing Bragg reflector*, Optics Letters **32**, 1117 (2007).

[47] J. P. Prineas, C. Cao, M. Yildirim, W. Johnston, and M. Reddy, *Resonant photonic band gap structures realized from molecular-beam-epitaxially grown InGaAs/GaAs Bragg-spaced quantum wells*, J. Appl. Phys. **100**, 063101 (2006).

[48] Mark J. Bloemer and Michael Scalora, *Transmissive properties of Ag/MgF2 photonic band gaps*, Appl. Phys. Lett. **72**, 1676 (1998).

[49] M. Scalora, M. J. Bloemer, A. S. Pethel, J. P. Dowling, C. M. Bowden, and A. S. Manka, *Transparent, metallo-dielectric, one-dimensional, photonic band-gap structures*, J. Appl. Phys. **83**, 2377 (1998).

[50] M. Sheik-Bahae, A. A. Said, T. Wei, D. J. Hagan, and E.W. Van Stryland, *Sensitive Measurement of Optical Nonlinearities Using a Single Beam*, IEEE J. Quantum Electron. **26**, 760 (1990).

[51] F. Hache, D. Ricard, C. Flytzanis, and U. Kreibig, *The Optical Kerr Effect in Small Metal Particles and Metal Colloids: The Case of Gold*, Applied Physics A **47**, 347 (1988).

[52] J.-Y. Bigot, V. Halté, J.-C. Merle, and A. Daunois, *Electron dynamics in metallic nanoparticles*, Chem. Phys. **251**, 181 (2000).

[53] W. S. Fann, R. Storz, H. W. K. Tom, and J. Bokor, *Elektron thermalization in gold*, Phys. Rev. B **46**, 13592 (1992).

[54] M. Perner, P. Bost, U. Lemmer, G. von Plessen, J. Feldmann, U. Becker, M. Mennig, M. Schmitt, and H. Schmidt, *Optically Induced Damping of the Surface Plasmon Resonance in Gold Colloids*, Phys. Rev. Lett. **78**, 2192 (1997).

[55] S. I. Anisimov, B. L. Kapeliovich, and T. L. Perel'man, *Electron emission from metal surfaces to ultrashort laser pulses*, Sov. Phys. JETP **39**, 375 (1974).

[56] S. G. Tikhodeev, A. L. Yablonskii, E. A. Muljarov, N. A. Gippius, and Teruya Ishihara, *Quasiguided modes and optical properties of photonic crystal slabs*, Physical Review B **66**, 045102 (2002).

[57] P. B. Johnson and R. W. Christy, *Optical Constants of the Noble Metals*, Phys. Rev. B **6**, 12 (1972).

[58] H. E. Elsayed-Ali, T. Juhasz, G. O. Smith, and W. E. Bron, *Femtosecond thermoreflectivity and thermotransmissivity of polycrystalline and single-crystalline gold films*, Phys. Rev. B **43**, 4488 (1991).

[59] Nir Rotenberg, A. D. Bristow, Markus Pfeiffer, Markus Betz, and H. M. van Driel, *Nonlinear absorption in Au films: Role of thermal effects*, Phys. Rev. B **75**, 155346 (2007).

Appendix

A. List of acronyms

1D one-dimensional

1DMDPC one-dimensional metal-dielectric photonic crystal

AOM acousto-optic modulator

BBO β-barium-borate

CCD charge-coupled device

EBPVD electron beam physical vapor deposition

ECR electron cyclotron resonance

FWHM full width at half maximum

GVD group-velocity dispersion

MQW multiple-quantum-well

NLSE nonlinear Schrödinger equation

PBG photonic band gap

PC photonic crystal

PECVD plasma-enhanced chemical vapor deposition

PMT photomultiplier tube

QW quantum well

RABR resonantly absorbing Bragg reflector

SC semiconductor

SMBE semiconductor Maxwell-Bloch equations

SPM self-phase modulation

XFROG cross-correlation frequency-resolved optical gating

B. List of figures

Acknowledgements

Finally, I would like to express my gratitude to all people who contributed to the success of this work. My personal thanks go to ...

- Prof. Dr. Harald Giessen for supervising me, for his support over many years, for the freedom he granted me during my work, for the confidence he put in my abilities, and for sharing his extraordinary passion for physics.
- Juniorprof. Dr. Markus Lippitz for his commendable support, the countless useful pieces of advice he gave me, as well as many fruitful discussions.
- Dr. Jürgen Kuhl for his support, advice and interest in my work even beyond his retirement.
- Prof. Dr. Peter Michler for kindly agreeing to be my second reviewer.
- Prof. Dr. Günter Wunner for kindly agreeing to be the head of the examination board.
- Dr. Martin Schaarschmidt, Dr. Jens Förstner, and Prof. Dr. Andreas Knorr for the collaboration and their theoretical contributions to our common projects.
- Dr. Thomas Zentgraf for being helpful in many occasions and for being my office colleague for such a long time.
- Dr. Nils Nielsen for all that I could learn from him.
- Armin Schulz and Peter Andler for technical support at the MPI.
- Dr. Liwei Fu, Hedi Gräbeldinger, Monika Ubl, Honcang Guo, and Na Liu for technical support in the MSL.

- Ewald Wagner for his expertise, patience, and help with vacuum systems.
- Prof. Dr. Sergei Tikhodeev for allowing me to use his scattering matrix program for the linear transmission spectra.
- Prof. Dr. Hyatt M. Gibbs and Prof. Dr. Galina Khitrova for providing the high-quality multiple-quantum-well Bragg structures.
- Gabi Feurle for her support in administrative matters.
- Sebastian Pricking for being my second-in-command ;) administrator and web master.
- my colleagues, particularly (in alphabetical order) Dr. Andre Christ, Tolga Ergin, Dr. Liwei Fu, Cornelius Grossmann, Hongcang Guo, Felix Hoos, Daniel Kunert, Na Liu, Dr. Todd Meyrath, Regina Orzekowsky, Markus Pfeiffer, Sebastian Pricking, Andreas Seidel, Tobias Utikal, and Dr. Thomas Zentgraf for the friendly working atmosphere and all the activities we shared.
- my parents Reinhild and Detlev for millions of things which I can impossibly recount here. I owe you so much.
- last but not least my beloved better half Katharina Benkert for being at my side for all the years and for helping me out of every "dip" of my motivation.

Lebenslauf

Persönliche Daten

Nachname	Höner zu Siederdissen
Vorname	Tilman
Geburtsdatum	27. September 1977
Geburtsort	Bielefeld

Schulbildung

1984–1988	Grundschule Sundern
1988–1997	Friedrichs-Gymnasium Herford
6/1997	Abitur Leistungsfächer: Physik, Mathematik

Zivildienst

8/1997–8/1998	Gemeinnützige Werkstatt für Behinderte Füllenbruchbetrieb Herford

Studium

8/1998–9/2003	Philipps-Universität Marburg Hauptfach: Physik

	Nebenfächer: Informatik, Mathematik
10/2000	Vordiplom
6/2002–9/2003	Externe Diplomarbeit am Max-Planck-Institut für Festkörperforschung, Stuttgart, in der Gruppe *Optik und Spektroskopie* geleitet von Dr. J. Kuhl
9/2003	Diplom Titel der Diplomarbeit: „Phasenaufgelöste Spektroskopie an CdSe" Erstgutachter: Prof. Dr. H. Gießen (Institut für Angewandte Physik, Universität Bonn) Zweitgutachter: Prof. Dr. W. Heimbrodt (Philipps-Universität Marburg)

Promotion

Seit 10/2003	Max-Planck-Institut für Festkörperforschung, Stuttgart, in der Gruppe *Optik und Spektroskopie* geleitet von Dr. J. Kuhl, ab 12/2006 in der Nachfolgegruppe *Ultraschnelle Nanooptik* geleitet von Juniorprof. Dr. Markus Lippitz. Erstgutachter: Prof. Dr. H. Gießen (4. Physikalisches Institut, Universität Stuttgart) Zweitgutachter: Prof. Dr. P. Michler (Institut für Halbleiteroptik und Funktionelle Grenzflächen, Universität Stuttgart)